nature chemical biology

Article

Membrane-domain compartmentalization of active GPCRs by β-arrestins through PtdIns(4,5)P$_2$ binding

Ritsuki Kuramoto[1], Tatsuya Ikuta [1], Carlo Marion C. Carino[1], Kouki Kawakami [1,5], Miisha Kushiro[1], Chihiro Watanabe[1], Yasunori Uchida[2,6], Mitsuhiro Abe [3], Yasushi Sako [3], Tomohiko Taguchi[2], Masataka Yanagawa [1,3] & Asuka Inoue [1,4] ✉

Upon ligand-induced activation, G-protein-coupled receptors (GPCRs) recruit β-arrestins (βarrs) to the plasma membrane, where phosphatidylinositol 4,5-bisphosphate (PtdIns(4,5)P$_2$) stabilizes the GPCR–βarr complex. Although PtdIns(4,5)P$_2$ is reported to form nanoscale clusters, the spatiotemporal dynamics of how the GPCR–βarr–PtdIns(4,5)P$_2$ complex assembles and organizes in living cells remain unexplored. Here we demonstrate that multiple PtdIns(4,5)P$_2$-binding sites on βarrs cooperatively promote GPCR–βarr assembly in membrane domains. Using molecular dynamics simulations, we identify a noncanonical (NC) PtdIns(4,5)P$_2$-binding site, distinct from the known canonical site. Biochemical assays confirm that both sites are essential for βarr binding to PtdIns(4,5)P$_2$-containing liposomes, while NanoBiT assays reveal synergistic contributions of both sites for βarr recruitment in living cells. Notably, single-molecule imaging demonstrates that the NC site is required for the rapid accumulation of the GPCR–βarr–PtdIns(4,5)P$_2$ complex into immobile membrane domains upon ligand stimulation. Collectively, our findings highlight how multivalent βarr–PtdIns(4,5)P$_2$ interactions drive GPCR–βarr compartmentalization, adding complexity to GPCR signaling dynamics.

Arrestins bind to ligand-activated G-protein-coupled receptors (GPCRs) and have critical roles in spatiotemporal regulations of GPCR signaling such as GPCR internalization and scaffolding of signaling effector proteins. Among the four arrestin subtypes encoded in the mammalian genome, β-arrestin1 (βarr1) and βarr2 are ubiquitously expressed while the other subtypes are exclusively expressed in the retinal tissue[1]. The two βarrs are responsible for internalization of numerous GPCRs by building clathrin-coated structures (CCSs) on the plasma membrane[2]. Foll

owing GPCR internalization, βarrs dissociate from GPCRs in intracellular vesicles such as the endosome, thereby allowing GPCRs to be recycled to the plasma membrane.

Spatiotemporal regulation of GPCR membrane transport depends on the strength of the interaction between GPCRs and βarrs. These interactions are primarily influenced by the phosphorylation state of GPCR C-terminal tails[3–5]. In class A GPCRs, which have a phosphorylated C-terminal tail with weak affinity for βarrs, βarrs rapidly dissociate from

[1]Graduate School of Pharmaceutical Sciences, Tohoku University, Sendai, Japan. [2]Laboratory of Organelle Pathophysiology, Department of Integrative Life Sciences, Graduate School of Life Sciences, Tohoku University, Sendai, Japan. [3]Cellular Informatics Laboratory, RIKEN Cluster for Pioneering Research, Wako, Japan. [4]Graduate School of Pharmaceutical Sciences, Kyoto University, Kyoto, Japan. [5]Present address: Research Center for Advanced Science and Technology, The University of Tokyo, Tokyo, Japan. [6]Present address: Division of Molecular Target and Gene Therapy Products, National Institute of Health Sciences, Kawasaki, Japan. ✉e-mail: iaska@tohoku.ac.jp

the GPCRs at the endosome, resulting in their eventual recycling to the plasma membrane. Conversely, class B GPCRs, characterized by a phosphorylated C-terminal tail that strongly binds βarrs, exhibit a slower recycling to the cell surface because of prolonged βarr association.

Recent research has revealed that the strength of the GPCR–βarr interaction is influenced not only by the interaction between βarrs and phosphorylated GPCR C termini but also by the βarr interaction with membrane lipids[4,6]. βarrs interact with membrane lipids at several sites. Firstly, βarrs form hydrophobic interactions with membrane lipids through C-edge loops[6]. The insertion of these loops into the membrane upon stimulation by ligand-activated GPCRs is thought to stabilize the active-like structure of βarr. Moreover, even in the absence of GPCR activation, βarrs spontaneously translocate to the plasma membrane and position themselves through insertion of the C-edge loops, subsequently binding to GPCRs through lateral diffusion[7]. Secondly, βarrs bind to membrane phospholipid phosphatidylinositol 4,5-bisphosphate (PtdIns(4,5)P$_2$) through its middle region of the C-domain (hereafter, we term this site the canonical (C) site). Our previous study showed that a PtdIns(4,5)P$_2$ can increase GPCR–βarr complex stability[4]. We further found that class A GPCRs are less efficacious than class B GPCRs in recruiting PtdIns(4,5)P$_2$-binding-site βarr mutants. This phenomenon is explained by the distinct affinity of GPCR C-terminal tails for βarrs; in class B GPCRs, the presence of abundant GPCR phosphorylation sites in their C-terminal tails compensates for the weakened GPCR–βarr affinity caused by PtdIns(4,5)P$_2$-binding deficiency.

Studies using total internal reflection fluorescence (TIRF) microscopy have demonstrated nonuniform distribution of GPCRs and βarrs on the plasma membrane. Upon ligand stimulation, GPCRs are accumulated in confined membrane domains including CCSs, decreasing the population of receptors that freely diffuse outside the membrane domains[8–10]. Single-molecule imaging in βarr1/2-deficient cells revealed that βarr binding is responsible for changes in the diffusion dynamics of GPCRs[11]. When βarr binds tightly to ligand-activated and phosphorylated GPCRs, the GPCR–βarr complex translocates to the membrane domain. On the other hand, when bound to a less phosphorylated GPCR such as β1AR, βarr can spontaneously dissociate from the receptor and migrate to the membrane domains alone[7,12]. However, to the best of our knowledge, no previous study has reported simultaneous single-molecule imaging of βarr and PtdIns(4,5)P$_2$ on the plasma membrane; consequently, the relationship between PtdIns(4,5)P$_2$ and the membrane domains where GPCRs and/or βarrs are accumulated remains to be elucidated.

In this study, we identified a novel PtdIns(4,5)P$_2$-binding site on βarr, distinct from the previously known C site. Using molecular simulations, biochemical assays and single-molecule imaging, we found that both sites cooperatively enhance GPCR–βarr complex formation and localization to membrane domains. These findings reveal that multivalent PtdIns(4,5)P$_2$ binding regulates GPCR signaling compartmentalization.

Results

Interactions with PtdIns(4,5)P$_2$ at the tip of the βarr C-domain

We explored for a potential PtdIns(4,5)P$_2$-binding site in βarr structures other than the previously characterized C PtdIns(4,5)P$_2$ site. βarrs have many positively charged residues on the surface of the membrane-facing side, which may interact with the negatively charged headgroup of PtdIns(4,5)P$_2$ (Fig. 1a)[13]. The positively charged C site residues (K232, R236 and K250 in βarr1 and K233, R237 and K251 in βarr2) are located in the dented middle part of the arc-shaped C-domain (Extended Data Fig. 1a,b). Other positively charged residues are located at the C-domain tips, including C-edge loops (190-FLMSDKPL-197 in βarr1 and 191-FLMSDRSL-198 in βarr2 and 330-SRGGLLGDLASS-341 in βarr1 and 331-SRGG-334 in βarr2). Because the C-edge loops are positioned closer to the membrane than the C site when the cytosolic βarr

is positioned adjacent to a planar lipid bilayer, we hypothesized that the positively charged residues at the C-domain tips may be involved in PtdIns(4,5)P$_2$ binding.

We performed all-atom molecular dynamics (MD) simulations to examine occurrences of PtdIns(4,5)P$_2$-binding events around the positively charged residues at the C-domain tips and the C site of βarr. On the basis of our previous study demonstrating that the loss of GPCR C-terminal phosphorylation necessitates PtdIns(4,5)P$_2$ binding of βarr to facilitate βarr recruitment, we used a V2RΔC (ref. 14), which lacks the serine-rich and threonine-rich C-terminal tail, as a model receptor. Using previously determined structures of the V2R–G$_s$ complex[15] and the M2 muscarinic receptor–βarr1 complex[16], we modeled a V2RΔC–βarr2 complex. We embedded the transmembrane region of the V2RΔC–βarr2 complex into a 1-palmitoyl-2-oleoyl-*sn*-glycero-3-phosphatidylcholine (POPC) bilayer supplemented with 5 mol.% PtdIns(4,5)P$_2$ molecules in the inner leaflet. Within 500 ns of three independent replicas of MD simulations, with each starting from randomly placed PtdIns(4,5)P$_2$ molecules (Extended Data Fig. 2a and Supplementary Fig. 1), PtdIns(4,5)P$_2$ molecules were found to interact with the C site residues and the C-domain tip residues, with specificity toward the two basic residues of the C-edge loops (Fig. 1b,c, Extended Data Fig. 2b and Supplementary Fig. 2). Quantitative interaction analysis showed that four C-domain tip residues (R196, K227, K230 and R332) remained in contact with PtdIns(4,5)P$_2$ molecules for more than half of the MD simulation trajectories, exceeding the duration of interaction observed at the C site (Fig. 1c). Among the four residues, R332 was consistently bound to PtdIns(4,5)P$_2$ throughout most of the simulation time. Concomitantly, in a previous crystal structure study[17], K227 and R332 were shown to interact with an inositol hexakisphosphate (InsP$_6$) molecule. Hereafter, we refer to the cluster of the four residues (R196, K227, K230 and R332 of βarr2) in the C-domain tips as the noncanonical site (NC) site (Fig. 1b,c).

PtdIns(4,5)P$_2$ binding at the NC site during the simulation stabilized a distinct βarr2 conformation that shifted toward an active-like state upon subsequent binding at the C site, consistent with experimental data (Supplementary Note 1). Even in the absence of GPCR, βarr2 frequently engaged PtdIns(4,5)P$_2$ at the NC site during the simulation, with the resulting conformations displaying greater diversity compared to the GPCR-bound condition (Supplementary Note 2). Collectively, our MD simulations identified that the NC site, positioned distinctly from the C site, can potentially contribute to the modulation of βarr2 structural dynamics.

The NC and C site dependence of βarr–PtdIns(4,5)P$_2$ membrane binding

We next experimentally investigated whether the NC site would be involved in binding to membrane PtdIns(4,5)P$_2$. To perform a biochemical experiment using the NC-site and C-site mutants, we expressed and purified βarr1 with or without substitutions at the C site (a triple mutant containing K232Q, R236Q and K250Q; C-3Q) or the NC site (a quadruple mutant containing K195Q, K226Q, K229Q and R331Q; NC-4Q). At first, we examined functionality of the purified βarr proteins to undergo conformational changes upon phosphorylated peptide using a Fab30 pulldown assay[18]. We incubated purified βarr1 with V2R phosphorylated peptide (V2Rpp) and subjected the samples to Fab30 pulldown. NC-4Q βarr1 exhibited an interaction with Fab30 upon binding to V2Rpp, similar to WT and C-3Q βarr1 (Extended Data Fig. 3a,b and Supplementary Note 3). These results suggest that βarr1 NC-4Q retains the capacity of undergoing functional activation upon phosphorylated GPCR engagement.

After confirming the functionality of the purified βarr1 mutants, we next investigated their ability to bind to membrane PtdIns(4,5)P$_2$. Purified βarr1 was then mixed with 1,2-dioleoyl-*sn*-glycero-3-phosphatidylcholine (DOPC) liposomes supplemented with or without 10 mol.% PtdIns(4,5)P$_2$ (Fig. 2a). After ultracentrifugation, pellets
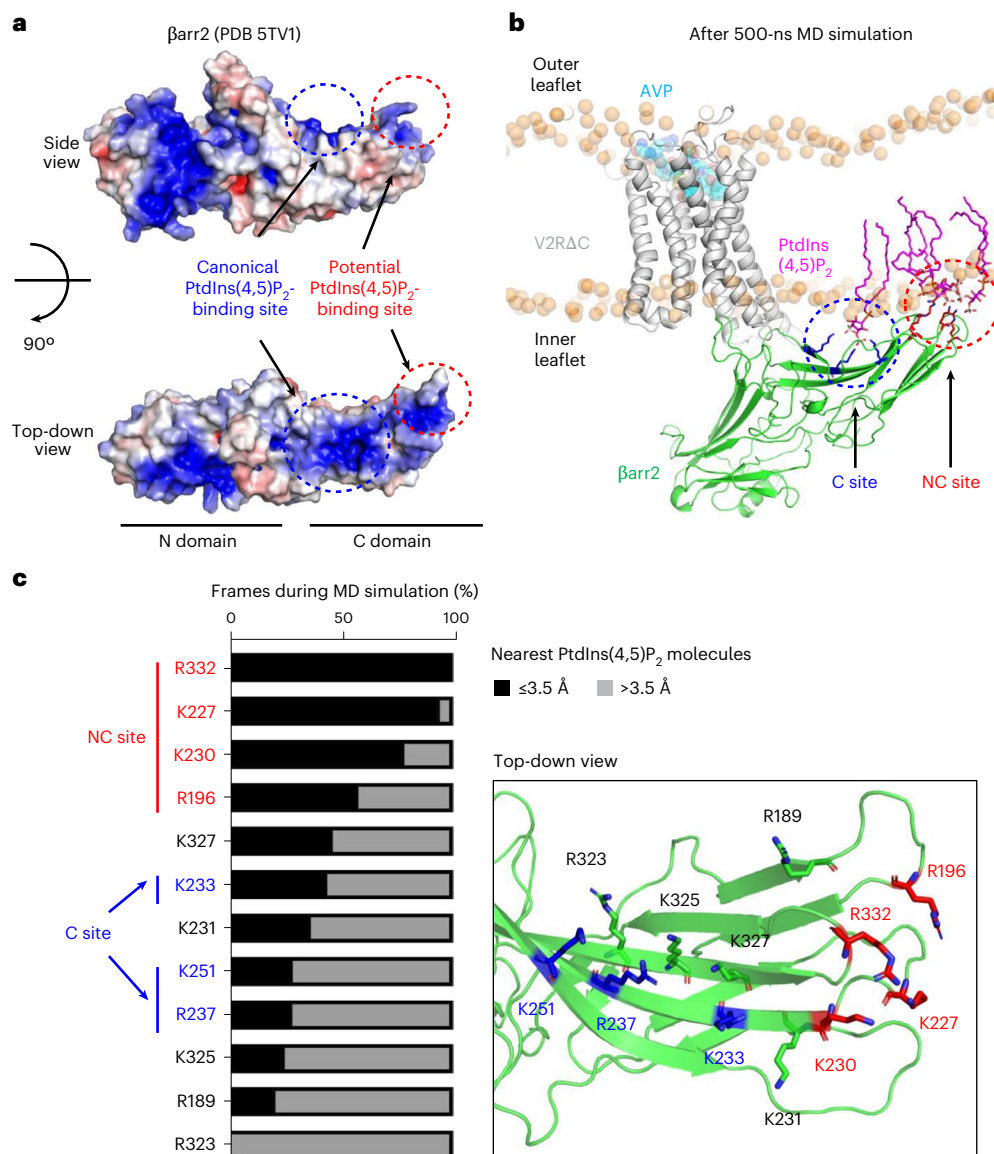
Fig. 1 | Identification of PtdIns(4,5)P$_2$ interaction at the tip regions of the βarr C-domain by MD simulation. a, Active βarr2 structure (PDB 5TV1). The molecular surface is colored according to the electrostatic potential, ranging from blue (+5 kT/e) to red (−5 kT/e), where kT is the thermal energy and e is the elementary charge. **b**, Snapshot of V2RΔC–βarr2 complex structure after 500-ns MD simulation. Blue, C PtdIns(4,5)P$_2$-binding site. Red, NC PtdIns(4,5)P$_2$-binding site. **c**, Left, analysis of βarr2–PtdIns(4,5)P$_2$ interaction in MD simulation. The percentage of time PtdIns(4,5)P$_2$ interacted with basic residues in the C-domain of βarr2 during three replicas of 500-ns MD simulations. The criterion for interaction was defined as the distance between atoms within 3.5 Å. Right, top-down view of the βarr2 C-domain, highlighting the basic residues analyzed. The C site and NC site are colored in blue and red, respectively.

of liposome-bound βarrs and the remaining supernatant were collected and quantified by SDS–PAGE (Fig. 2b,c)[19]. In the DOPC-only liposome condition, precipitated amounts of βarr1 were almost as low as those in the nonliposome control, showing a lack of association with the DOPC-only liposome by the wild-type (WT) βarr1 and βarr1 mutants. When using the PtdIns(4,5)P$_2$-supplemented liposome, we observed enhanced precipitation in the WT βarr1. In contrast, the C-site-mutant βarr1 and the NC-site-mutant βarr1 showed almost no liposome-binding activity. A fluorescence polarization assay using soluble BODIPY-labeled PtdIns(4,5)P$_2$ showed a clear reduction in binding for C-3Q, whereas its binding level of NC-4Q was similar to that of the WT (Supplementary Fig. 3). This difference may be attributable to variations in PtdIns(4,5)P$_2$ states between the soluble, monomer form and the membrane-embedded state. This interpretation is further supported by surface plasmon resonance (SPR) experiments using PtdIns(4,5)P$_2$-containing liposomes, which showed decreased levels

of PtdIns(4,5)P$_2$ binding in both mutants compared to the WT (Supplementary Fig. 4). Together, these results demonstrate that both the C site and the NC site have substantial roles in PtdIns(4,5)P$_2$ binding, particularly in a bilayer environment.

Given the locations of the NC site at the edge of the C-domain, including R196 and R332 on the C-edge loops, we hypothesized that the interaction between the NC site and PtdIns(4,5)P$_2$ promotes insertion of the C-edge loop into the membrane. To assess how NC site–PtdIns(4,5)P$_2$ interactions influence βarr membrane insertion, we conducted five independent 2-µs coarse-grained (CG) simulations for WT and NC-site-mutant βarr2 in PtdIns(4,5)P$_2$-containing membranes (Extended Data Fig. 4). In all trajectories (five of five runs), WT βarr2 inserted its C-edge loop into the membrane (Extended Data Fig. 4b,c). For the NC-4Q βarr2, the C-edge loop of the NC-4Q βarr2 occasionally (two of five runs) oriented away from the membrane, suggesting unstable membrane association (Extended Data Fig. 4b,c).
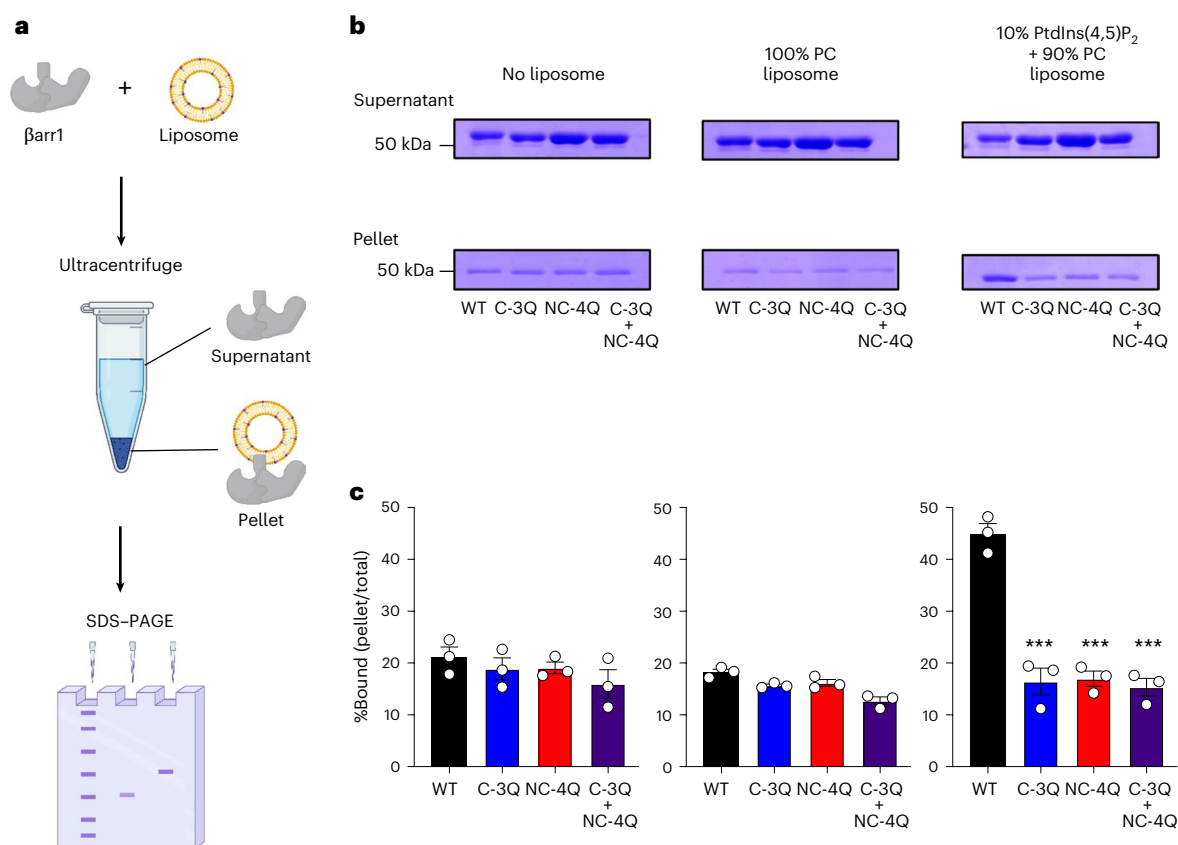
Fig. 2 | Lack of PtdIns(4,5)P$_2$-containing liposome binding in NC-site-mutant βarr. a, Schematic representation of the liposome-binding assay. **b**, Assessment of βarr and PtdIns(4,5)P$_2$ interactions through the precipitation of liposomes containing PtdIns(4,5)P$_2$ and βarr. SDS–PAGE was performed to analyze the results of βarr1 mixed with liposomes under various conditions: no liposome (−), 100% PC and a mixture of 10% PtdIns(4,5)P$_2$ + 90% PC. **c**, Quantification of the liposome-binding assay. The values of percentage bound (pellet/total) are shown in a bar graph. Bars and error bars represent the mean and s.e.m., respectively, of three independent experiments. For the statistical analyses, data were analyzed by one-way ANOVA followed by the Dunnett's test for multiple-comparison analysis. ***$P < 0.001$ versus WT. The schematic was created with BioRender.com.

To quantify insertion of the C-edge loop (amino acid position R332 for WT and Q332 for NC-4Q) of WT and NC-4Q βarr2 into the membrane, we defined C-edge loop insertions as interactions within the distance of 5 Å. The analysis showed that 74.9% of frames in WT exhibited the membrane interaction, whereas only 49.1% of frames in the NC-4Q did (Extended Data Fig. 4c,e). We further analyzed the interactions between PtdIns(4,5)P$_2$ and the NC site residues (amino acid positions R196, K227, K230 and R332 in the WT; amino acid positions Q196, Q227, Q230 and Q332 in NC-4Q). In the WT, at least two NC site residues were bound to PtdIns(4,5)P$_2$ in 71.9% of frames, whereas, in NC-4Q, this was observed in only 2.48% of frames (Extended Data Fig. 4d,f). Additionally, in WT βarr2, PtdIns(4,5)P$_2$ binding was detected in most frames where C-edge loop insertion occurred. These findings indicate that NC site–PtdIns(4,5)P$_2$ interactions have a crucial role in facilitating C-edge loop insertion into the membrane.
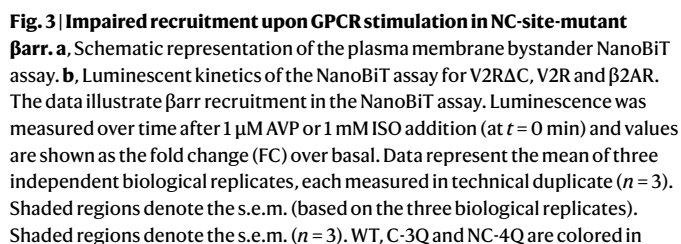
Synergistic effects of the C and NC sites on translocation

To examine the roles of the NC site in living cells, we next performed a bystander NanoBiT βarr recruitment assay for both βarr subtypes[20,21]. In this assay, GPCR-stimulated recruitment of βarrs to the plasma membrane was monitored through the use of SmBiT-fused βarrs and the LgBiT-fused CAAX-motif bystander (Fig. 3a). We first confirmed that expression levels of the C-3Q and the NC-4Q mutants were comparable to those of WT βarr1 and WT βarr2 (Extended Data Fig. 5a,b). We then measured agonist-induced recruitment of βarrs for representative class A GPCRs (V2RΔC and β2AR) and a representative class B GPCR (full-length V2R) (Fig. 3b). In both class A and class B GPCRs[4,5], we found

a slower association kinetics for the C-3Q and the NC-4Q mutants than WT βarrs (Fig. 3b,c and Extended Data Fig. 5c), consistent with previous findings in the C-3Q study[4]. When assessed at 15 min, an endpoint βarr recruitment measurement, both the C-3Q and the NC-4Q mutants showed impaired recruitment in the class A GPCRs as compared to the WT βarrs (Fig. 3b,d and Extended Data Fig. 5d). In the class B GPCR, both mutants were recruited to a similar extent to that of WT βarrs. These results indicate that, in a cellular context, PtdIns(4,5)P$_2$ binding to the NC site promotes βarr recruitment in both class A and class B GPCRs, with higher necessity for class A GPCRs. Notably, the effects of the C and NC sites on βarr recruitment by class A GPCRs are synergistic rather than additive (Fig. 3b–d), suggesting that the multivalent interaction with PtdIns(4,5)P$_2$ is essential for the stabilization of βarr on the plasma membrane as predicted by the MD simulation (Fig. 1b).

To determine whether the reduction in βarr NC-4Q recruitment is PtdIns(4,5)P$_2$ dependent, we also performed a NanoBiT βarr recruitment assay under conditions of synaptojanin (SYNJ) overexpression. SYNJ is a phosphatase that hydrolyzes PtdIns(4,5)P$_2$, thereby reducing the level of PtdIns(4,5)P$_2$ in the plasma membrane[22]. Upon V2R activation, the overexpression of SYNJ significantly decreased the rate of recruitment for both the WT and the C-3Q mutant to the level observed for the NC-4Q mutant without SYNJ overexpression (Extended Data Fig. 6a,b). Because the C-3Q mutant retains the NC site (Extended Data Fig. 6c), the observed decrease in βarr recruitment rate upon SYNJ overexpression suggests that NC site-dependent recruitment relies on PtdIns(4,5)P$_2$.

On the basis of these findings, we next examined whether the NC-4Q mutant adopts an activated conformation in cells using a

Fig. 3 | Impaired recruitment upon GPCR stimulation in NC-site-mutant βarr. a, Schematic representation of the plasma membrane bystander NanoBiT assay. **b**, Luminescent kinetics of the NanoBiT assay for V2RΔC, V2R and β2AR. The data illustrate βarr recruitment in the NanoBiT assay. Luminescence was measured over time after 1 μM AVP or 1 mM ISO addition (at $t = 0$ min) and values are shown as the fold change (FC) over basal. Data represent the mean of three independent biological replicates, each measured in technical duplicate ($n = 3$). Shaded regions denote the s.e.m. (based on the three biological replicates). Shaded regions denote the s.e.m. ($n = 3$). WT, C-3Q and NC-4Q are colored in

black, blue and red, respectively. **c**,**d**, Quantification of the NanoBiT assay. Bar graph showing the initial rate of recruitment (**c**) and endpoint recruitment (**d**) for WT, C-3Q and NC-4Q βarr1 and βarr2. For each experiment, data were normalized to the WT response. Bars and error bars are the mean and s.e.m, respectively, of three independent experiments with each performed duplicate. For the statistical analyses, data were analyzed by one-way ANOVA followed by Dunnett's test for multiple-comparison analysis. NS, not significantly different between the groups. *$P < 0.05$, **$P < 0.01$ and ***$P < 0.001$ versus WT. The schematic was created with BioRender.com.

NanoBiT-Ib30 assay[9]. Ib30 is a single-chain fragment variant of Fab30 that recognizes active conformation. Upon V2R activation, WT βarrs exhibited increased interaction with Ib30. NC-4Q βarr1 displayed a slightly lower interaction with Ib30 compared to WT (Extended Data Fig. 7a,b). We note that this reduction was proportional to the decrease in its recruitment (Extended Data Fig. 7c). Ib30 responses were markedly diminished when using the V2RΔC construct, underscoring the importance of GPCR phosphorylation for βarr conformational activation (Supplementary Fig. 5). These results suggest that the NC-4Q mutant retains an ability to adopt the activated conformation once it is recruited to the phosphorylated GPCR.

To pin down contributions of the individual residues in the NC site, we performed the NanoBiT βarr recruitment assay using single, double and triple βarr mutants (Extended Data Fig. 8). For triple mutants, any combination of the four substitutions showed almost identical recruitment to that of the NC-4Q. For single mutants, βarr2 R332Q (R331Q in βarr1) showed reduced recruitment to V2RΔC compared to WT βarrs, while βarr2 R196Q (K195Q in βarr1) showed mostly unchanged recruitment to V2RΔC compared to WT βarrs. We note that the functional effects of the single mutants were generally consistent with the MD simulation. In the NC site, R332 engaged with PtdIns(4,5)P$_2$ for the longest time while R196 engaged for the shortest time (Fig. 1c). The results suggest that the four residues at the NC site contribute to recruitment responses with varying degrees but collectively support βarr recruitment in class A GPCRs.

NC-site-dependent rapid βarr clustering in confined domains

We performed three-color single-molecule time-lapse imaging to simultaneously analyze the spatiotemporal dynamics of V2R, βarr (WT, C-3Q or NC-4Q) and PtdIns(4,5)P$_2$ on the plasma membrane. SF650-labeled V2R, mEGFP-fused βarr2 (WT, C-3Q or NC-4Q) and JF549-labeled PLCδ-PH (PtdIns(4,5)P$_2$ probe) were expressed in βarr1/2-deficient HEK293 cells and monitored by a multicolor TIRF microscopy system[23]. Ligand-dependent changes in particle density, diffusion dynamics and intensity histograms (as an index of cluster size) were analyzed from 300-frame (33 fps) videos of the same cells taken every 5 min (Fig. 4 and Supplementary Video 1). Upon arginine vasopressin (AVP) stimulation, the membrane translocation of WT and C-3Q βarr2 was observed within 5 min, forming bright immobile clusters, whereas NC-4Q βarr2 showed a delayed recruitment by V2R (Fig. 4a and Extended Data Fig. 9f). In association with the degree of membrane translocation of βarr2, brighter and slower-diffusing particles of V2R and PLCδ-PH increased on the plasma membrane (Supplementary Video 1).

To quantify the effects of the C-3Q and the NC-4Q mutants on the diffusion dynamics of V2R, βarr2 and PtdIns(4,5)P$_2$, we performed a hidden Markov model (HMM)-based clustering analysis of trajectories[9]. Comparison of the lower bounds of the variational Bayesian method suggested that the trajectory of each particle can be classified into three or four diffusion states, depending on the cells and molecules (Extended Data Fig. 9g). To apply the same number of states across molecules, we used the four-state model (immobile, slow, medium and fast) for comparison. Immobile, slow and medium states of all probes showed confined diffusion modes, as represented by concave-down plots of mean square displacement (MSD) versus Δt, suggesting entrapment in membrane domains with different confinement lengths (immobile, 50–100 nm; slow, 100–200 nm; medium, 200–400 nm; Extended Data Fig. 9h). In contrast, the fast states for all probes showed linear plots of MSD versus Δt, suggesting that the molecules diffuse freely outside the membrane domains.

We compared the time-dependent changes in the diffusion and oligomerization states of βarr2 WT and mutants using intensity histograms of each diffusion state (Fig. 4b). Before AVP stimulation, WT and mutant βarr2 exhibited the highest proportion of the loosely confined diffusion state (medium) (Extended Data Fig. 10a). WT βarr2 showed relatively higher fractions of the restricted diffusion states (immobile and slow) than the mutants. βarr2 mutants showed a higher fraction of the simple diffusion state (fast), which was particularly pronounced in the NC-4Q mutant. The peaks in the intensity histogram were mostly ~200 photons, regardless of diffusion states (Extended Data Fig. 10b), suggesting a similar oligomeric state distribution. These results suggested that the multivalent interactions between βarr2 and PtdIns(4,5)P$_2$ through the C site and the NC site are responsible for the confinement of βarr2 molecules in membrane domains even before activation by GPCRs. For WT and mutant βarr2, an increase in restricted diffusion states (immobile and slow) and a decrease in the less confined diffusing population (medium and fast) were observed after AVP stimulation (Fig. 4c,f and Extended Data Fig. 10a,b). Significant increases in the peak intensity of the histograms were observed only in the restricted diffusion states (immobile and slow), indicating the higher-order clustering of βarr2 in membrane domains (Supplementary Fig. 6). The kinetics of the diffusion and oligomeric state changes were significantly slower in the NC-4Q mutant, consistent with the NanoBiT βarr recruitment assay.

Accompanying the higher-order clustering of βarr2 in membrane domains upon AVP stimulation, the diffusion states of V2R and PtdIns(4,5)P$_2$ were similarly altered in WT and C-3Q βarr2 but not in NC-4Q βarr2 coexpressing cells (Fig. 4d–h, Extended Data Fig. 10c–f and Supplementary Figs. 7 and 8). V2R and PLCδ-PH in the restricted diffusion states (immobile and slow) were increased 15 min after AVP stimulation in WT and C-3Q βarr2 coexpressing cells. Along with the diffusion state fraction change, the peak in the intensity histogram of the immobile state of PLCδ-PH showed a rightward shift 15 min after AVP stimulation in cells coexpressing WT or C-3Q βarr2 but not in the NC-4Q mutant (Extended Data Fig. 10e,f and Supplementary Fig. 8). These results indicate that the NC site affects not only βarr itself but also the diffusion dynamics of V2R and PtdIns(4,5)P$_2$, which may facilitate formation of PtdIns(4,5)P$_2$-rich membrane domains to accumulate activated V2R molecules. Collectively, these single-molecule dynamic data demonstrate that the NC site of βarr2 has an impact on the membrane distributions of βarr2 molecules, V2R and PtdIns(4,5)P$_2$.

NC-site-dependent V2R–βarr coclustering in PtdIns(4,5)P$_2$ domains

To evaluate a possible role of the NC site in the accumulation of the V2R–βarr2 complex in PtdIns(4,5)P$_2$-rich membrane domains, we examined colocalization among V2R, βarr2 and PtdIns(4,5)P$_2$. We calculated the colocalization index (CI) of the three pairs of particles following a previous report[24]. In the first pair (βarr2 and PLCδ-PH), AVP stimulation significantly increased the CI for both WT and C-3Q βarr2, whereas NC-4Q βarr2 showed a negligible change in CI (Fig. 5a), indicating that the NC site is more important for interaction with PtdIns(4,5)P$_2$ than the C site. In the second pair (V2R and βarr2), WT and C-3Q βarr2 exhibited an elevation in CI upon AVP stimulation (Fig. 5b). Unexpectedly, NC-4Q βarr2 did not show a significant increase in CI. This suggests that V2R can recruit NC-4Q βarr2 to the plasma membrane, albeit slowly, but cannot form a stable complex on the plasma membrane. In other words, NC-4Q βarr2 is catalytically recruited by V2R to the plasma membrane and forms clusters alone in the membrane domain (Fig. 4 and Supplementary Video 2). In the third pair (V2R and PLCδ-PH), AVP stimulation similarly increased the CI in both WT and C-3Q but not NC-4Q βarr2 (Fig. 5c). These results indicate that the NC site also contributes to the agonist-dependent compartmentalization of V2R in a PtdIns(4,5)P$_2$-rich membrane domain.

We note that while PLCδ-PH binding to PtdIns(4,5)P$_2$ might compete with βarr interactions, our experimental design uses PLCδ-PH as a sparse sampling tool. Given the high density of PtdIns(4,5)P$_2$ in the plasma membrane (~10,000 molecules per μm^2)[25] and especially in clustered membrane domains (~1,000 molecules per domain)[26], only a small fraction (<0.01%) is detected by PLCδ-PH under our conditions to achieve sparse density (<1 particle per μm^2) required for single-molecule detection. Therefore, the colocalization analysis between βarr and PLCδ-PH serves as a probabilistic measure of their
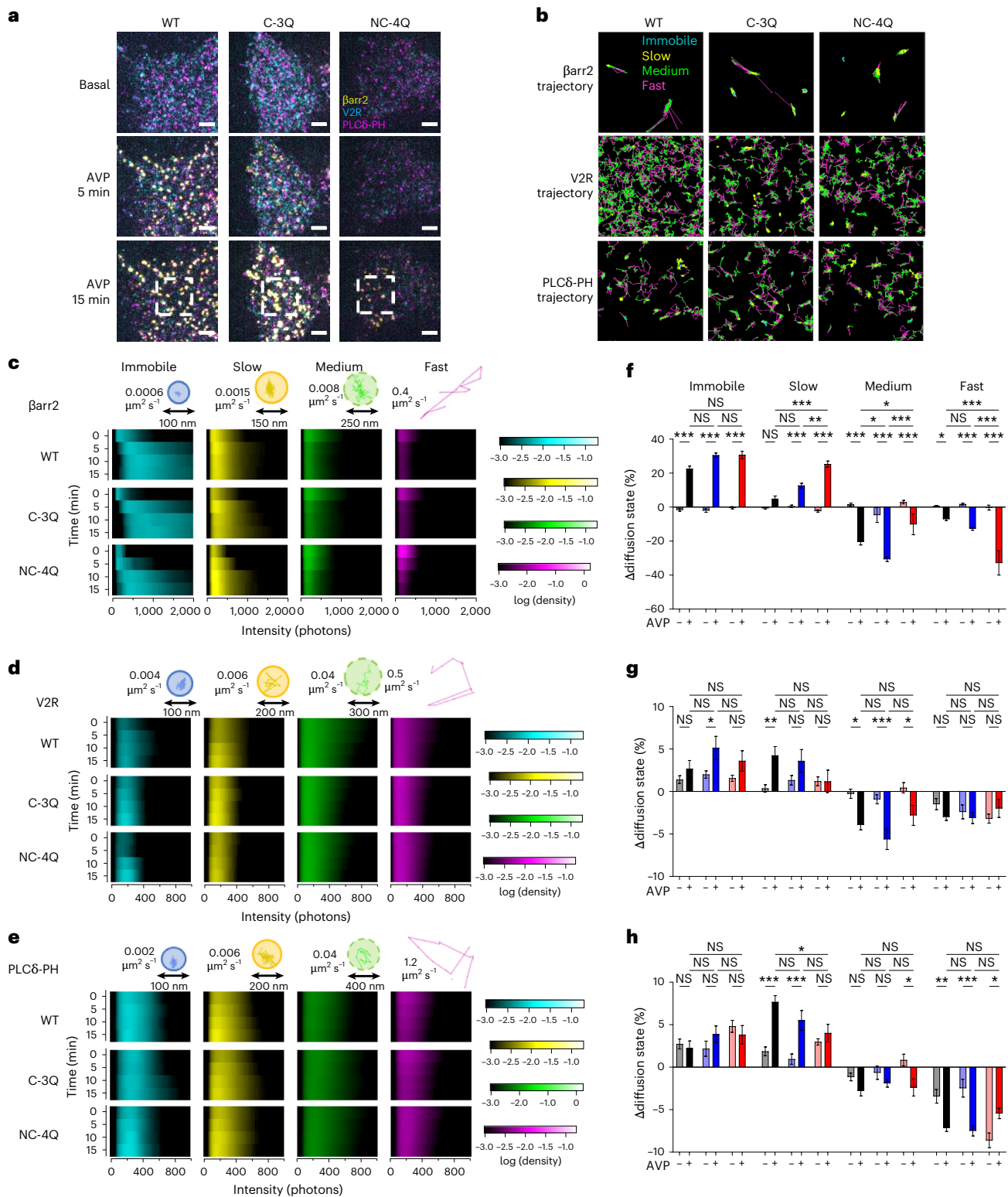
Fig. 4 | Delayed immobile cluster formation of βarr in the NC-site-mutant βarr. a, Representative TIRF microscopic image of Δβarr1/2 cells expressing EGFP–βarr2 (WT, C-3Q or NC-4Q), SF650-labeled V2R (cyan) and JF549-labeled PLCδ-PH (magenta) before AVP stimulation (basal), after 5-min AVP stimulation and after 15-min AVP stimulation. Scale bar, 3 μm. **b**, Enlarged view of **a** and representative trajectories of four diffusion states (immobile, cyan; slow, yellow; medium, green; fast, magenta) of βarr2, V2R and PLCδ-PH molecules after 15-min AVP stimulation. Scale bars, 0.5 μm (βarr2) and 1 μm (V2R and PLCδ-PH). **c–e**, Heat map showing the time course of intensity histograms for each diffusion state in βarr2 (**c**), V2R (**d**) and PLCδ-PH (**e**) molecules. The particle density with each intensity was displayed according to a color scale. **f–h**, The difference

in fractions of the four diffusion states in βarr2 (**f**), V2R (**g**) and PLCδ-PH (**h**) molecules between basal conditions and after 15-min ligand stimulation. WT, C-3Q and NC-4Q are colored in black, blue and red, respectively. WT AVP (−), $n = 19$; WT AVP (+), $n = 36$; C-3Q AVP (−), $n = 19$; C-3Q AVP (+), $n = 32$; NC-4Q AVP (−), $n = 18$; NC-4Q AVP (+), $n = 23$; n represents individual cells analyzed across two independent biological replicates. AVP (−), vehicle stimulation; AVP (+), AVP stimulation. In **a**,**b**, representative images from the groups are shown. In **c–e**, bars and error bars represent the mean and s.e.m., respectively. Statistical significance was calculated using a two-way ANOVA followed by Tukey's test for multiple-comparison analysis. *$P < 0.05$, **$P < 0.01$ and ***$P < 0.001$.
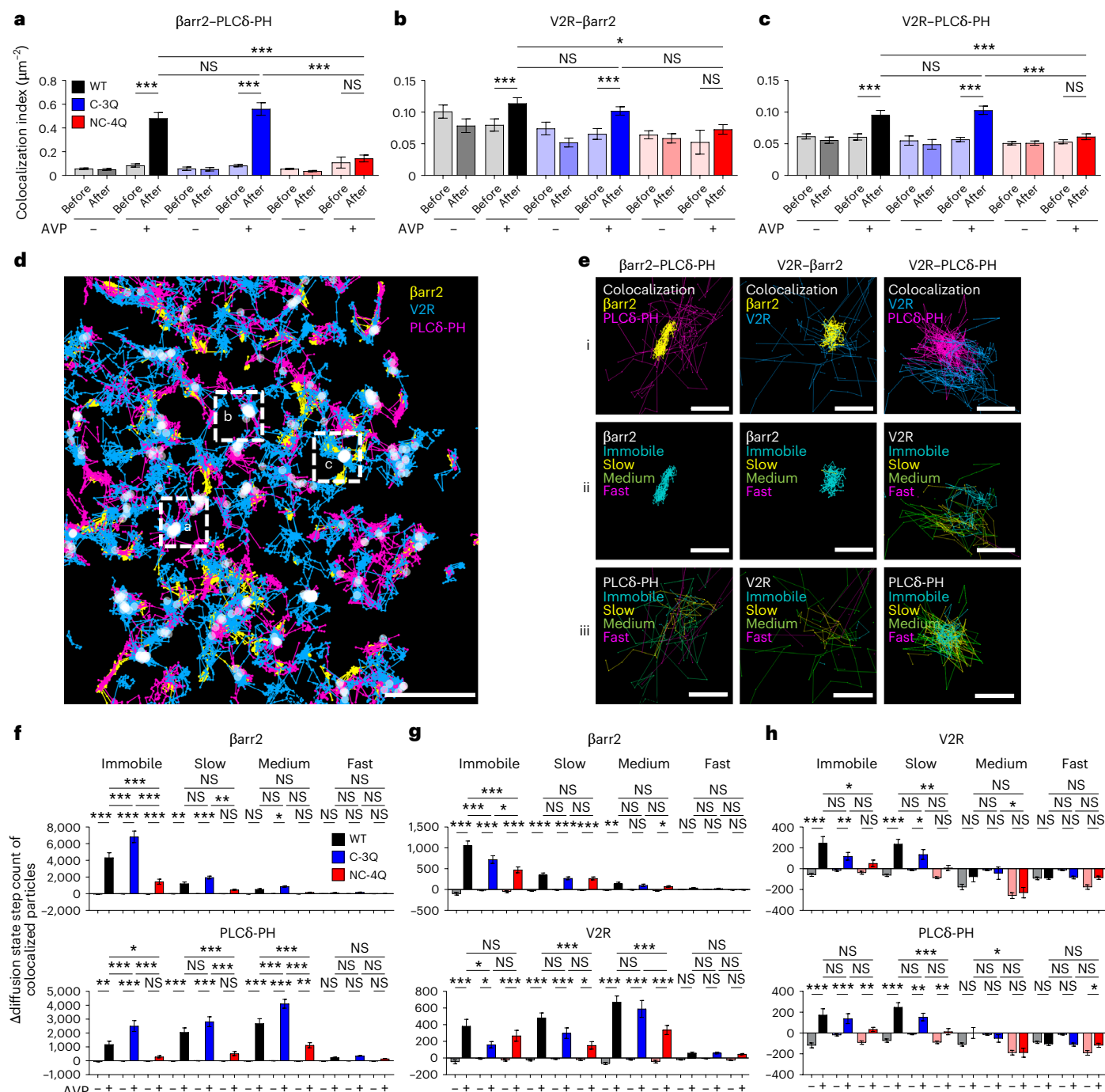
Fig. 5 | Impaired formation of GPCR–βarr complex and PtdIns(4,5)P₂ domain by NC-site-mutant βarr. a–c, CI of the three particle pairs under basal conditions (pre) and after 15 min of AVP stimulation (post) in both AVP-treated and vehicle-treated conditions: βarr2–PLCδ-PH (**a**), V2R–βarr2 (**b**) and V2R–PLCδ-PH (**c**). WT, C-3Q and NC-4Q are represented in black, blue and red, respectively. **d**, Merged images of βarr2 (yellow), V2R (cyan) and PLCδ-PH (magenta) particle trajectories. Trajectories of these three molecules were projected on the colocalized coordinates (round markers). Scale bars, 1 μm. **e**, Enlarged views of the area enclosed by the white dotted liners of **d**. Colocalization trajectories of βarr2–PLCδ-PH, V2R–βarr2 and V2R–PLCδ-PH. Colocalization of two molecules (i) and four diffusion state of each molecule (ii, iii). Scale bars, 1 μm.

f–h, The difference in diffusion state step count of colocalized molecules among the three particle pairs between basal conditions and after 15 min of ligand stimulation: βarr2–PLCδ-PH (**f**), V2R–βarr2 (**g**) and V2R–PLCδ-PH (**h**). WT AVP (−), n = 19; WT AVP (+), n = 36; C-3Q AVP (−), n = 19; C-3Q AVP (+), n = 32; NC-4Q AVP (−), n = 18; NC-4Q AVP (+), n = 23; n represents individual cells analyzed across two independent biological replicates. AVP (−), vehicle stimulation; AVP (+), AVP stimulation. In **a–c,f–h**, bars and error bars represent the mean and s.e.m., respectively. Statistical significance was calculated using a two-way ANOVA followed by Tukey's test for multiple-comparison analysis. *P < 0.05, **P < 0.01 and ***P < 0.001.

presence within the same membrane domains; higher CI indicates spatial convergence, while lower CI suggests spatial separation.

To evaluate the diffusion state during each molecular interaction, we quantified the AVP-dependent change in the number of colocalization steps for each diffusion state. For the first pair (βarr2 and PLCδ-PH), AVP stimulation increased the interactions between immobile βarr2 and confined diffusing PtdIns(4,5)P₂ (immobile, slow and medium) but did not significantly increase the interactions between
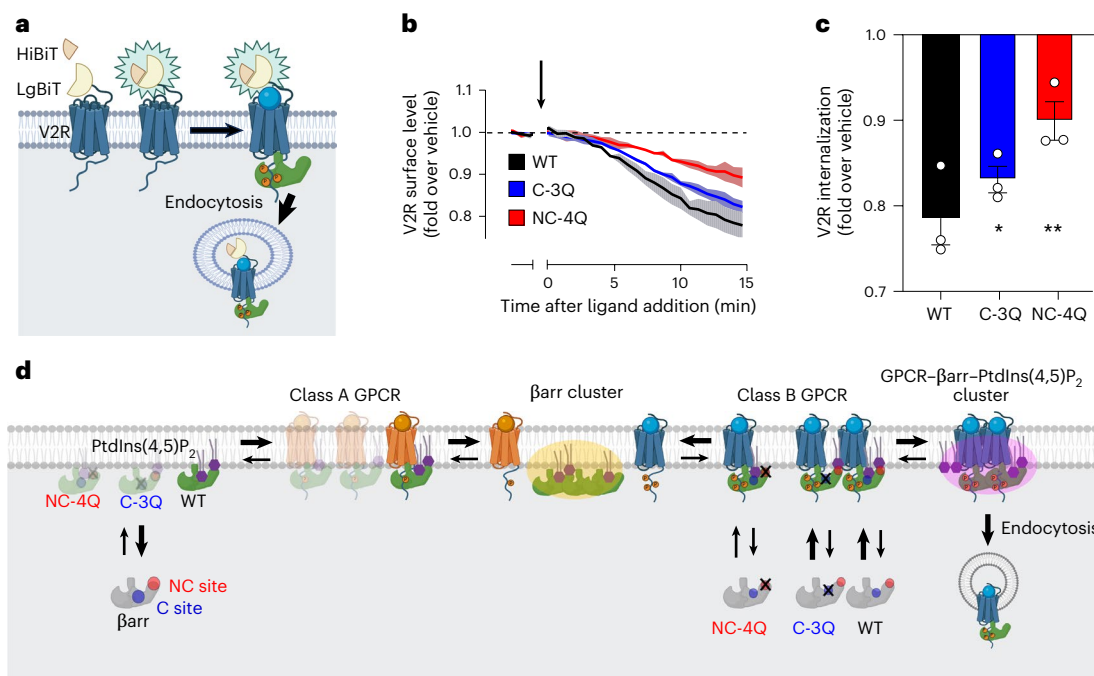
Fig. 6 | The multivalent PtdIns(4,5)P$_2$ interaction of βarr alters the dynamics and localization of both GPCR and βarr. a, Luminescent kinetics of the HiBiT-based V2R-internalization assay. **b**, Luminescence was measured over time after 1 µM AVP addition (at $t = 0$ min) and values are shown as the FC over vehicle at each time point. Data represent the mean of three independent biological replicates, each measured in technical duplicate ($n = 3$). Shaded regions denote the s.e.m. ($n = 3$). WT, C-3Q and NC-4Q are colored in black, blue and red, respectively. **c**, Quantification of the HiBiT-based V2R-internalization assay at 13–15 min after ligand addition. **d**, Proposed model of GPCR–βarr dynamics through PtdIns(4,5)P$_2$ binding. Before agonist stimulation, βarrs spontaneously preassociate with the plasma membrane through PtdIns(4,5)P$_2$ binding to both the C site and the NC site. In class A, βarrs transiently bind to GPCRs and dissociate from GPCRs, leading to the formation of βarr clusters at the plasma membrane. In class B GPCRs, βarrs bind continuously to GPCRs and PtdIns(4,5)P$_2$ through the C site and the NC site, resulting in the formation of GPCR–βarr–PtdIns(4,5)P$_2$ clusters and promoting effective endocytosis. The NC-site-mutant βarrs destabilize the GPCR–βarr complex, causing βarrs to accumulate in βarr clusters instead of GPCR–βarr–PtdIns(4,5)P$_2$ clusters. In **c**, bars and error bars are the mean and s.e.m., respectively, of three independent experiments with each performed duplicate. For the statistical analyses, data were analyzed by one-way ANOVA followed by Dunnett's test for multiple-comparison analysis. *$P < 0.05$, **$P < 0.01$ and ***$P < 0.001$. The schematic was created with BioRender.com.

freely diffusing βarr2 and PtdIns(4,5)P$_2$ (Fig. 5f). NC-4Q showed a significantly lower increase in the colocalization steps than WT and C-3Q and the detected colocalization was mainly between immobile βarr2 and medium mobile PtdIns(4,5)P$_2$. These results suggest that the WT and C-3Q βarr2 cluster can stabilize loosely confined PtdIns(4,5)P$_2$-rich membrane domains but NC-4Q βarr2 cannot. Similar colocalization patterns were observed in the second pair (V2R and βarr2) but AVP stimulation significantly increased the colocalization steps in WT and mutant βarr2 (Fig. 5g). This is consistent with the phosphorylated C-tail of V2R directly recruiting βarrs from the cytosol. Consistent with these observations, the increase in colocalization steps between V2R and PtdIns(4,5)P$_2$ was significantly detected in the restricted diffusion states (immobile and slow) in WT and C-3Q βarr2 coexpressing cells but not NC-4Q (Fig. 5h). Collectively, our data strongly indicate that the NC sites have a critical role in stabilizing both V2R and βarrs to the PtdIns(4,5)P$_2$-rich membrane domain.

At last, we measured ligand-induced endocytosis of V2R as a functionality of βarrs. Inefficient formation of the V2R–βarr2–PtdIns(4,5)P$_2$ cluster in the NC-4Q βarr2-expressing cells suggests that the following receptor endocytosis would be reduced. We expressed βarr (WT, C-3Q or NC-4Q) and N-terminally LgBiT-tagged V2R in βarr1/2-deficient cells and performed a HiBiT-based receptor internalization assay (Fig. 6a). We found that the AVP-stimulated V2R-internalization response was slower in NC-4Q than WT and C-3Q βarr2 (Fig. 6b); therefore, the endocytic activity of NC-4Q βarr2 was smaller than that of WT and C-3Q βarr2 (Fig. 6c and Extended Data Fig. 7d). Additional single-molecule imaging revealed that CCSs and PtdIns(4,5)P$_2$-rich membrane domains are largely nonoverlapping (Supplementary Fig. 9), suggesting that

βarr-mediated PtdIns(4,5)P$_2$ domains outside CCSs may contribute to regulating GPCR internalization. In summary, our finding demonstrates that the NC site contributes more notably than the C site to PtdIns(4,5)P$_2$ interactions at the plasma membrane, facilitating GPCR accumulation in PtdIns(4,5)P$_2$-rich membrane domains and regulating endocytosis.

Discussion

The NC site of βarr promotes the formation of the GPCR–βarr cluster in 50–300-nm membrane domains, resulting in efficient GPCR endocytosis. Our study revealed that the cationic residues at the tip regions of the βarr C-domain, including the C-edge loop, serve as binders for anionic PtdIns(4,5)P$_2$ molecules in the plasma membrane. The single-molecule imaging revealed that the NC site, compared to the C site, significantly increases the accumulation of GPCRs and PtdIns(4,5)P$_2$ in the membrane domains where βarrs are highly condensed. Moreover, the HiBiT-based receptor internalization assay showed that the NC site promotes endocytosis. On the basis of our findings, we propose a model where the spatial localization of GPCR is regulated by βarrs and PtdIns(4,5)P$_2$ through the NC site (Fig. 6d). A small fraction of βarrs are spontaneously anchored to the plasma membrane through the C and NC sites. In a previous study[7], such spontaneous membrane recruitment and dissociation was documented by single-molecule imaging. Upon agonist stimulation, GPCRs recruit βarrs from the plasma membrane through lateral diffusion and/or directly from the cytoplasm, increasing higher-order clusters of βarrs. In some trafficking class A GPCRs, such as β1AR, βarrs transiently bind to GPCRs and are catalytically activated at the plasma membrane[12], where both the C and the NC sites

are required to maintain membrane tethering. On the other hand, in class B GPCRs, βarrs continuously bind to GPCRs and PtdIns(4,5)P$_2$ through multivalent binding sites to form cocondensates in the membrane domains. The NC-site-mutant βarrs change the behavior of class B GPCRs, including V2R, to a class A-like catalytic activation feature, indicating that the NC site is essential for stabilizing the GPCR–βarr complex at the plasma membrane even when the C-tail of the class B GPCR is phosphorylated by GPCR kinases (GRKs).

Our observations in living cells are consistent with the previous structural and biophysical studies showing that the C-edge loop is inserted into the membrane in vitro[6,27] and stabilizes the GPCR–βarr complex[4]. Previous in vitro single-molecule fluorescence resonance energy transfer analysis showed that both phosphorylation and agonist binding of GPCRs are important for the efficient activation of βarr (ref. [28]) and our results further indicate the importance of βarr–PtdIns(4,5)P$_2$ binding at the plasma membrane. Notably, our biochemical assays suggest that the contribution of basic residues in βarrs to PtdIns(4,5)P$_2$ binding depends on whether PtdIns(4,5)P$_2$ is in a soluble or membrane-embedded form, indicating that βarr–PtdIns(4,5)P$_2$ interactions are highly context dependent. Taken together, PtdIns(4,5)P$_2$ binding at the NC site likely precedes the C-edge loop insertion into the plasma membrane and these processes are essential for stable complex formation of the GPCR and βarrs, which promotes receptor desensitization and endocytosis.

The PtdIns(4,5)P$_2$ cluster in the inner leaflet of the plasma membrane acts as a platform for cell signaling. Our single-molecule observation showed that βarrs alter the dynamics of PtdIns(4,5)P$_2$, increasing the slow diffusion state with a confinement length of 200 nm. Because of their negative charge, PtdIns(4,5)P$_2$ molecules repulse each other and are less likely to form membrane domains without a factor to help accumulate them. The βarr-induced accumulation of PtdIns(4,5)P$_2$ within the confined diffusion state suggests that βarrs neutralize PtdIns(4,5)P$_2$'s negative charge, thereby promoting PtdIns(4,5)P$_2$ cluster formation in the membrane domain. Notably, no increase in PtdIns(4,5)P$_2$ confined diffusion was observed in NC-site-mutant βarr, underscoring the importance of the NC site in this process. Consistent with our finding, previous stimulated emission depletion microscopy demonstrated that the electrostatic interaction between syntaxin 1A and PtdIns(4,5)P$_2$ is essential for their cocluster formation in the 73-nm membrane domain, which regulates the neuronal exocytosis[29]. Single-molecule localization microscopy also visualized the existence of PtdIns(4,5)P$_2$ clusters (40–250 nm) in the inner leaflet of the plasma membrane, which couples to the sphingomyelin-rich lipid raft in the outer leaflet in a transbilayer manner, spatially regulating RhoA signaling on cytokinesis and EGFR signaling[30,31]. The spatiotemporal regulation of PtdIns(4,5)P$_2$ has an important role for initiation and maturation of endocytic machinery such as CCSs and caveolae[32,33]. Collectively, βarrs accumulate phosphorylated GPCRs and PtdIns(4,5)P$_2$ molecules through their multivalent cationic residues that neutralize the repulsion between negatively charged molecules, leading to efficient internalization of GPCRs by facilitating the initiation and maturation of these endocytic machineries.

In general, coaccumulation of signaling proteins in specific membrane domains is considered to be crucial for efficient signal transduction. For example, upon ligand stimulation, GPCRs coaccumulate with G proteins in a membrane domain and this process enhances G-protein activation[34]. Apart from GPCRs, receptor tyrosine kinases (RTKs) are known to translocate to membrane domains and induce efficient signal transduction. Accumulating evidence suggests that liquid–liquid phase separation is also a key mechanism underlying the compartmentalized signaling of RTKs at the plasma membrane, where the multivalent interaction between receptors and transducers promotes the condensate formation[35,36]. With respect to GPCR signaling, our previous study focusing on GRKs showed that ligand-activated GPCRs coaccumulate in membrane domains with GRKs[9]. While the GPCR–GRK-accumulated domain has not been further characterized in the context of membrane lipids, it is likely that GRKs are accumulated in PtdIns(4,5)P$_2$-rich membrane domains, as GRKs bind to PtdIns(4,5)P$_2$ through their PH domain. This hypothesis is also consistent with our previous observation that G$_q$ activation, which leads to a reduction in membrane PtdIns(4,5)P$_2$ by PLCβ, causes a spatial segregation of the preassembled complex of GPCR and GRK5/6 in the membrane domain. Given our current study showing that GPCRs, βarrs and PtdIns(4,5)P$_2$ accumulate in the membrane domains through multivalent interactions, we speculate that βarrs and GRKs act synergistically to induce efficient GPCR signaling in the PtdIns(4,5)P$_2$-rich domain. In this domain, GPCRs cocluster with GRKs and βarrs, undergo efficient phosphorylation by GRKs and tightly bind to βarr, which further accumulates PtdIns(4,5)P$_2$ molecules and recruits more GRKs.

In conclusion, we describe the NC PtdIns(4,5)P$_2$-binding site in βarrs. In contrast to the C site, the NC site has a role in coaccumulating GPCRs, βarrs and PtdIns(4,5)P$_2$ in a membrane domain. These findings provide an additional layer of spatiotemporal regulations of βarr–GPCR signaling.

Online content

Any methods, additional references, Nature Portfolio reporting summaries, source data, extended data, supplementary information, acknowledgements, peer review information; details of author contributions and competing interests; and statements of data and code availability are available at https://doi.org/10.1038/s41589-025-01967-4.

References

1. Komolov, K. E. & Benovic, J. L. G protein-coupled receptor kinases: past, present and future. *Cell. Signal.* **41**, 17–24 (2018).
2. Hanyaloglu, A. C. & Von Zastrow, M. Regulation of GPCRs by endocytic membrane trafficking and its potential implications. *Annu. Rev. Pharmacol. Toxicol.* **48**, 537–568 (2008).
3. Latorraca, N. R. et al. How GPCR phosphorylation patterns orchestrate arrestin-mediated signaling. *Cell* **183**, 1813–1825 (2020).
4. Janetzko, J. et al. Membrane phosphoinositides regulate GPCR–β-arrestin complex assembly and dynamics. *Cell* **185**, 4560–4573 (2022).
5. Oakley, R. H., Laporte, S. A., Holt, J. A., Caron, M. G. & Barak, L. S. Differential affinities of visual arrestin, βarrestin1, and βarrestin2 for G protein-coupled receptors delineate two major classes of receptors. *J. Biol. Chem.* **275**, 17201–17210 (2000).
6. Lally, C. C. M., Bauer, B., Selent, J. & Sommer, M. E. C-edge loops of arrestin function as a membrane anchor. *Nat. Commun.* **8**, 1–12 (2017).
7. Grimes, J. et al. Plasma membrane preassociation drives β-arrestin coupling to receptors and activation. *Cell* **186**, 2238 (2023).
8. Yanagawa, M. et al. Single-molecule diffusion-based estimation of ligand effects on G protein-coupled receptors. *Sci. Signal* **11**, eaao1917 (2018).
9. Kawakami, K. et al. Heterotrimeric G$_q$ proteins act as a switch for GRK5/6 selectivity underlying β-arrestin transducer bias. *Nat. Commun.* **13**, 487 (2022).
10. Beletkaia, E. et al. CXCR4 signaling is controlled by immobilization at the plasma membrane. *Biochim. Biophys. Acta* **1863**, 607–616 (2016).
11. Qin, G., Xu, J., Liang, Y. & Fang, X. Single-molecule imaging reveals differential AT1R stoichiometry change in biased signaling. *Int. J. Mol. Sci.* **25**, 374 (2024).
12. Eichel, K. et al. Catalytic activation of β-arrestin by GPCRs. *Nature* **557**, 381–386 (2018).
13. Huang, W. et al. Structure of the neurotensin receptor 1 in complex with β-arrestin 1. *Nature* **579**, 303–308 (2020).

14. Ghosh, E. et al. Conformational biosensors and domain-swapping reveal structural and functional differences between the β-arrestin isoforms. *Cell Rep.* **28**, 3287 (2019).

15. Wang, L. et al. Cryo-EM structure of the AVP–vasopressin receptor 2–G_s signaling complex. *Cell Res.* **31**, 932–934 (2021).

16. Staus, D. P. et al. Structure of the M2 muscarinic receptor–β-arrestin complex in a lipid nanodisc. *Nature* **579**, 297–302 (2020).

17. Chen, Q. et al. Structural basis of arrestin-3 activation and signaling. *Nat. Commun.* **8**, 1–13 (2017).

18. Cahill, T. J. et al. Distinct conformations of GPCR–β-arrestin complexes mediate desensitization, signaling, and endocytosis. *Proc. Natl Acad. Sci. USA* **114**, 2562–2567 (2017).

19. Uchida, Y. et al. Intracellular phosphatidylserine is essential for retrograde membrane traffic through endosomes. *Proc. Natl Acad. Sci. USA* **108**, 15846–15851 (2011).

20. Dixon, A. S. et al. NanoLuc complementation reporter optimized for accurate measurement of protein interactions in cells. *ACS Chem. Biol.* **11**, 400–408 (2016).

21. Xu, Z. et al. Structural basis of sphingosine-1-phosphate receptor 1 activation and biased agonism. *Nat. Chem. Biol.* **18**, 281–288 (2022).

22. Field, S. J. et al. PtdIns(4,5)P_2 functions at the cleavage furrow during cytokinesis. *Curr. Biol.* **15**, 1407–1412 (2005).

23. Yoda, T., Sako, Y., Inoue, A. & Yanagawa, M. Four-color single-molecule imaging system for tracking GPCR dynamics with fluorescent HiBiT peptide. *Biophys. Physicobiol.* **21**, e210020 (2024).

24. Yanagawa, M. & Sako, Y. Workflows of the single-molecule imaging analysis in living cells: tutorial guidance to the measurement of the drug effects on a GPCR. *Methods Mol. Biol.* **2274**, 391–441 (2021).

25. Wills, R. C. & Hammond, G. R. V. PI(45)P2: signaling the plasma membrane. *Biochem J.* **479**, 2311–2325 (2022).

26. Wen, Y., Vogt, V. M. & Feigenson, G. W. PI(4,5)P2 clustering and its impact on biological functions. *Annu. Rev. Biochem.* **90**, 681–707 (2021).

27. Zhai, R. et al. Distinct activation mechanisms of β-arrestin-1 revealed by ^{19}F NMR spectroscopy. *Nat. Commun.* **14**, 7865 (2023).

28. Asher, W. B. et al. GPCR-mediated β-arrestin activation deconvoluted with single-molecule precision. *Cell* **185**, 1661–1675 (2022).

29. Van Den Bogaart, G. et al. Membrane protein sequestering by ionic protein–lipid interactions. *Nature* **479**, 552–555 (2011).

30. Abe, M. et al. A role for sphingomyelin-rich lipid domains in the accumulation of phosphatidylinositol-4,5-bisphosphate to the cleavage furrow during cytokinesis. *Mol. Cell. Biol.* **32**, 1396 (2012).

31. Abe, M., Yanagawa, M., Hiroshima, M., Kobayashi, T. & Sako, Y. Bilateral regulation of EGFR activity and local PI(4,5)P_2 dynamics in mammalian cells observed with superresolution microscopy. *eLife* **13**, e101652 (2024).

32. Antonescu, C. N., Aguet, F., Danuser, G. & Schmid, S. L. Phosphatidylinositol-(4,5)-bisphosphate regulates clathrin-coated pit initiation, stabilization, and size. *Mol. Biol. Cell* **22**, 2588 (2011).

33. Fujita, A., Cheng, J., Tauchi-Sato, K., Takenawa, T. & Fujimoto, T. A distinct pool of phosphatidylinositol 4,5-bisphosphate in caveolae revealed by a nanoscale labeling technique. *Proc. Natl Acad. Sci. USA* **106**, 9256 (2009).

34. Sungkaworn, T. et al. Single-molecule imaging reveals receptor–G protein interactions at cell surface hot spots. *Nature* **550**, 543–547 (2017).

35. López-Palacios, T. P. & Andersen, J. L. Kinase regulation by liquid–liquid phase separation. *Trends Cell Biol.* **33**, 649–666 (2023).

36. Yanagawa, M. & Shimobayashi, S. F. Multi-dimensional condensation of intracellular biomolecules. *J. Biochem.* **175**, 179–186 (2024).

Methods

Reagents and plasmids

AVP and isoproterenol (ISO) were purchased from Sigma-Aldrich. Tetramethylrhodamine (TMR)-labeled HiBiT peptide (TMR–HiBiT: TMR-VSGWRLFKKIS) was synthesized in Genscript. SaraFluor650-labeled Flag–HiBiT[23] (SF650–FiBiT: SF650-DYKDDDDKGDGSV SGWRLFKKIS) was synthesized and purified in RIKEN CBS (RRD peptide synthesis service). TMR–HiBiT and SF650–FiBiT were dissolved in dimethyl sulfoxide (DMSO; Wako) and used as stock solutions. The concentration of the stock solutions was quantified on the basis of absorbance in PBS.

For the liposome-binding assay, the βarr1 construct was derived from the long splice variant of human with all cysteine residues substituted (C59V, C125S, C140L, C150V, C242V, C251V and C269S). This construct was modified with an N-terminal 6xHis-tag, followed by a tobacco etch virus protease cleavage site (ENLYFQS). The sequence was codon-optimized for expression in *Escherichia coli* and cloned into the pET-15b vector. Plasmids for the NanoBiT βarr recruitment assay were previously described[37]. For NanoBiT assays, human full-length βarr1 and βarr2 were N-terminally fused to a small fragment (SmBiT) of the NanoBiT luciferase with a 15-aa flexible linker (GGSGGGGSGGSSSGG) and human full-length V2R was N-terminally fused to the FLAG epitope tag with the preceding HA-derived signal sequence and a 15-aa flexible linker (MKTIIALSYIFCLVFADYKDDDDKGGSGGGGSGGSSSGGG, FLAG epitope tag underlined; FLAG–V2R). For the PM-localizing tag, LgBiT was C-terminally fused to the CAAX motif derived from human KRAS (SSSGGGGKKKKKKSKTKCVIM) through the same flexible linker (LgBiT–CAAX). For PtdIns(4,5)P$_2$ depletion, mCherry was N-terminally fused to human SYNJ and inserted into the pDEST vector. For the Ib30 binding assay, LgBiT was fused to the single-chain fragment variant of Fab30 through the same flexible linker (Lg–Ib30). For single-molecule imaging, βarr2 was N-terminally fused to SmBiT and EGFP with a 13-aa flexible linker (GFP–βarr2) and inserted into the pcDNA3 vector. Human full-length V2R was N-terminally fused to the large fragment (LgBiT) of NanoBiT luciferase with a 15-aa flexible linker (LgBiT–V2R) and inserted into pEGFP-N1 vector. PLCδ-PH were N-terminally fused to the HaloTag with a 15-aa flexible linker (Halo–PLCδ-PH) and inserted into the pHalo vector.

Unless otherwise indicated, all constructs were inserted into the pCAGGS expression plasmid vector. The βarr mutant constructs were generated by an in-house-modified QuikChange site-directed mutagenesis kit. The specific oligonucleotide primers used for site-directed mutagenesis are listed in Supplementary Table 1.

MD simulations

The initial coordinates of the V2RΔC–βarr2 complex (V2R: residues 32–342, βarr2: residues 1–352) were prepared with MODELLER 9.25 using the structure of the muscarinic M2 receptor–βarr1 complex (Protein Data Bank (PDB) 6U1N) and V2R–G$_s$ complex (PDB 7KH0)[15,16]. On the basis of these atomic coordinates, the CG model was generated with the MARTINI version 2.2 force field using the script martinize. py available from the MARTINI web site (http://www.cgmartini.nl/).

CG MD simulations were performed in the GROMACS simulation package with the standard Martini version 2.2 simulation setup. The CG model was centered in a periodic simulation box with dimensions $16 \times 16 \times 16$ nm^3. POPC molecules and PtdIns(4,5)P$_2$ molecules were randomly placed in the lower leaflet around the protein and the system was solvated and neutralized to a concentration of 150 mM NaCl. After minimization with the steepest descent algorithm, 1.1-µs simulations were performed at 310 K. At the end of the CG model simulations, proteins and lipids were converted to all-atom models by Martini's backmapping scheme.

All-atom models were solvated with TIP3P water and 150 mM NaCl using the CHARMM36m force field. MD simulations were performed with GROMACS 2020.4. The system was first energy-minimized until

the maximum force dropped below 1,000 kJ mol^{-1} nm^{-1}. First equilibrations were performed at 310 K for 100 ps under NVT conditions with 1,000 kJ mol^{-1} nm^{-2} restraints for heavy atoms in the proteins and ligands. Second equilibrations with restraints were performed for 1 ns under NPT conditions at 1.0 bar using semi-isotropic pressure coupling. Constant temperature and pressure were maintained using the Nosé–Hoover method and the Parrinello–Rahman method, respectively. Long-range electrostatics were calculated using the particle mesh Ewald method. Production runs were performed for 500 ns.

The βarr2 NC-4Q model was generated from βarr2 WT using MODELLER 9.25. These models were then converted into CG models in the same manner as described above. The PtdIns(4,5)P$_2$-containing membrane was also constructed following the same procedure. The CG βarr2 WT or NC-4Q model was centered in a periodic simulation box with dimensions of $12 \times 12 \times 16$ nm^3. The system was solvated and neutralized to a concentration of 150 mM NaCl. After energy minimization using the steepest descent algorithm, production runs were conducted for 2 µs. Both all-atom and CG simulation trajectories were analyzed and visualized by using PyMOL (version 2.6.0a0), MDTraj 1.9.6, NumPy 1.21.1 and Matplotlib 3.4.2.

Analysis of membrane equilibration in the MD simulation

The area per lipid was calculated by multiplying the x and y dimensions of the simulation box and dividing by the number of lipids. In this calculation, the area occupied by V2RΔC was subtracted from the total membrane area before normalizing by the number of lipid molecules. The diffusion coefficient for lateral lipid diffusion was calculated on the basis of the MSD phosphorus atoms of POPC using the Einstein relation: $MSD(t) = 4Dt$. The membrane thickness was calculated on the basis of the distance difference between the phosphorus atoms of POPC in the inner and outer leaflets. The potential energy was calculated on the basis of the sum of bonded and nonbonded interaction energies obtained from the GROMACS energy output.

Protein expression and purification

His-tagged βarr1 (WT, C-3Q, NC-4Q and C-3Q + NC-4Q) was expressed in *E. coli* BL21(DE3) cells cultured in lysogeny broth. Cells were grown at 37 °C until the optical density at 600 nm reached 0.7–0.8. Cells were then transferred to 18 °C and induced with 100 µM IPTG. Cells were harvested after overnight induction. Cell pellets were resuspended in lysis buffer (20 mM Tris-HCl pH 8.0, 150 mM NaCl, 10% glycerol and 10 mM imidazole) and lysed by sonication. Cell lysates were then centrifuged (15,000g, 1 h, 4 °C) and the supernatant was applied to Ni-NTA resin and batch-incubated for 1.5 h at 4 °C. The resin was washed with ten column volumes of wash buffer (20 mM Tris-HCl pH 8.0, 150 mM NaCl, 10% glycerol and 20 mM imidazole). The protein was then eluted with five column volumes of elute buffer (20 mM Tris-HCl pH 8.0, 150 mM NaCl, 10% glycerol and 200 mM imidazole) and dialyzed overnight in 100 volumes of dialysis buffer (20 mM Tris-HCl pH 8.0, 150 mM NaCl, 10% glycerol). The protein was then purified by SEC using a Superdex 200 increase 10/300 GL column (GE Healthcare) with dialysis buffer. Purified protein was concentrated using a 30-kDa spin concentrator and aliquots were flash-frozen in liquid nitrogen and stored at −80 °C.

Coimmunoprecipitation (co-IP) assay

Co-IP was performed to evaluate the activation of WT, C-3Q, NC-4Q and C-3Q + NC-4Q βarr1 in the presence of V2Rpp by evaluating the interaction between βarr1 proteins and Fab30 (refs. 18,38). Then, 1.5 µg of βarr1 proteins were incubated with 2.5 µg of Fab30 with tenfold molar excess of V2Rpp for 1 h at room temperature (27 °C) in 200 µl of binding buffer (20 mM HEPES pH 7.4, 150 mM NaCl and 10% glycerol). Next, 21 µl of the reaction mixture was collected as loading samples and 7 µl of 4× SDS sample buffer was added. Subsequently, 5 µl of pre-equilibrated protein L-agarose MAG2 beads (Ptotenova, P-054-1) were added to the reaction

mixture and incubated for an additional 1 h at room temperature, which was followed by three washes with 500 µl of washing buffer (20 mM HEPES pH 7.4, 150 mM NaCl, 10% glycerol and 0.003% DDM). Elution was taken with 25 µl of 1× SDS sample buffer. Interaction of βarr1 with Fab30 in the presence of V2Rpp was visualized using western blotting as described below. The intensities of individual bands were quantified with National Institutes of Health (NIH) ImageJ (version 1.53e).

Liposome-binding assay

His-tagged βarr1 (WT, C-3Q, NC-4Q and C-3Q + NC-4Q) was expressed in *E. coli* BL21(DE3) cells. The proteins were purified using a HisTrap HP column (GE Healthcare) according to the manufacturer's instructions. The liposome-binding assay in this study followed previously described methods[19,39]. PC (840053) and PtdIns(4,5)P_2 (840046) were purchased from Avanti. Liposomes were composed of either 100 mol.% PC or a mixture of 90 mol.% PC and 10 mol.% PtdIns(4,5)P_2. These lipid mixtures were dried under nitrogen gas and hydrated in 25 mM HEPES pH 7.5, 100 mM NaCl and 0.5 mM EDTA for 1 h at 37 °C and vortexed for 1 min. To remove aggregated proteins, purified proteins were subjected to centrifugation at 100,000g for 15 min at 4 °C. Then, 10 µg of proteins were incubated with 65 nmol (50 µg) of liposomes in buffer (50 µl) for 15 min at room temperature and the mixture was centrifuged at 100,000g for 30 min at 20 °C. The resultant supernatant and pellet were subjected to SDS–PAGE and the gels were stained with Coomassie blue. The intensities of individual bands were quantified with NIH ImageJ.

Fluorescence anisotropy measurements

BODIPY–PtdIns(4,5)P_2 (Echelon Biosciences) was dissolved to a stock concentration of 1 mM in 50 mM HEPES pH 7.4 and used at a final concentration of 4 nM in the assay. For the arrestin measurements, a 3.2-fold dilution series was made from a stock of βarr1 (full length), yielding five samples with final concentrations ranging from 100 µM to 1 µM. A control sample containing buffer only was included to measure the free anisotropy of BODIPY–PtdIns(4,5)P_2. After mixing the BODIPY–PtdIns(4,5)P_2 with arrestin or buffer, samples were incubated for 1 h at room temperature before measurements. Samples were measured in five 20-ml replicates in a black 384-well plate on a Tecan Infinite M1000 (Tecan Life Sciences), using an excitation wavelength of 530 nm, an emission wavelength of 573 nm and bandwidths of 5 nm. The obtained data were fitted to a one-site total binding model $Y = \text{bottom} + ð\text{top bottom}Þ = 1 + 10\text{HS}\cdot\log ð\text{EC}_{50} XÞ$, where HS denotes the Hill slope.

Preparation of large unilamellar vesicles (LUVs)

Multilamellar vesicles (MLVs) composed of DOPC:PI(4,5)P_2 (95:5) were subjected to three freeze–thaw cycles by alternately placing the sample vial in a liquid nitrogen bath and a warm water bath. The MLVs were passed through polycarbonate filters with a 100-nm pore size (Cytiva, 800309) at least 20 times with an extruder (Mini Extruder, Avanti Polar Lipids).

SPR analysis

As previously described in detail[40], SPR experiments were carried out in a Biacore X 100 Plus Package (Cytiva) in single-cycle kinetic assay mode at 25 °C. The L1 sensor chip (Cytiva) was used because the chip can maintain lipid bilayer structure. Before use, the chip was rinsed with two injections of 40 mM *n*-octyl-β-D-glucoside. LUVs composed of DOPC:Chol:PI(4,5)P_2 (49:49:2) were immobilized onto the L1 sensor chip by injecting 1 mM LUVs in running buffer (PBS) including 1% glycerol for 60 s. After the sensor chip was washed, five series of different concentrations of the recombinant proteins were injected for 60 s and solutes were allowed to dissociate for 300 s. The sensor chip surface regeneration was performed with sequential injections of 40 mM *n*-octyl-β-D-glucoside.

Cell culture and transfection

HEK293A cells were obtained from Thermo Fisher Scientific (R70507, RRID: CVCL_6910). βarr1/2-deficient HEK293A cells (Δβarr1/2) were generated from parental HEK293A cells using CRISPR–Cas9-mediated gene editing, as previously described[41]. All cell lines were tested for *Mycoplasma* contamination using a PCR-based assay and confirmed to be negative. No further authentication was performed during this study but HEK293A cells were sourced from a certified vendor with a certificate of analysis. None of the cell lines used in this study are listed as misidentified or cross-contaminated in the ICLAC database (https://iclac.org/databases/cross-contaminations/). These cells were maintained in DMEM (Nissui Pharmaceutical) supplemented with 5% FBS (Gibco, Thermo Fisher Scientific) and penicillin–streptomycin–glutamine (complete DMEM) at 37 °C in a humidified incubator containing 5% CO_2. Transfection was performed using polyethylenimine (PEI) solution (PEI Max, Polysciences). For the NanoBiT βarr recruitment assay and western blot, HEK293A cells were seeded in a six-well culture plate at cell density of $2–3 × 10^5$ cells per ml in 2 ml of complete DMEM and cultured for 1 day. A transfection solution was prepared by combining plasmid solution diluted in 100 µl of Opti-MEM (Gibco, Thermo Fisher Scientific) and 100 µl of Opti-MEM containing 5 µl of 1 mg ml^{-1} PEI (Opti-MEM-PEI). The transfected cells were further incubated for 24 h before being subjected to each assay.

NanoBiT assays

For the βarr recruitment assay, plasmid transfection was performed in a six-well plate with a mixture of 100 ng of SmBiT–βarr, 500 ng of LgBiT–CAAX and 200 ng of V2R plasmids (volumes denote per well). For the PtdIns(4,5)P_2 depletion assay, an additional 1000 ng of mCherry–SYNJ was included in the transfection mixture. For the Ib30 assay, plasmid transfection was performed in a six-well plate with a mixture of 100 ng of SmBiT–βarr, 500 ng of LgBiT–Ib30 and 200 ng of V2R or V2RΔC plasmids. After 24-h incubation, the transfected cells were harvested with EDTA–PBS, centrifuged and suspended in 2 ml of 0.01% BSA and 5 mM HEPES (pH 7.4)-containing HBSS (assay buffer). The cell suspension was dispensed on a 96-well white culture plate at a volume of 80 µl per well and added with 20 µl of 50 µM coelenterazine (Angene) diluted in the assay buffer. After 2-h incubation in the dark at room temperature, the plate was read for its baseline luminescence using SpectraMax L plate reader by SoftMax Pro 7.1.2 (Molecular Devices). Then, 20 µl of 6× ligands serially diluted in the assay buffer were manually added. The plate was read for 15 min with an interval of 20 s and integration time of 0.18 s at room temperature. The luminescence counts over 13–15 min after ligand addition were averaged and the fold change value was calculated on the basis of the initial count. Agonist-induced βarr recruitment was fitted to a four-parameter sigmoidal concentration–response curve with the Hill slope constrained to an absolute value less than 1.5 using the following equation: $Y = \text{bottom} + (\text{top} − \text{bottom})/(1 + 10^{((\log\text{EC50} − X) × \text{Hill slope})})$ (GraphPad Prism 10).

HiBiT-based receptor internalization assay

V2R internalization was measured using a HiBiT-based receptor internalization assay[9]. A plasmid mixture of 50 ng of LgBiT–V2R, 25 ng of EGFP–βarr2 (WT, C-3Q or NC-4Q) and 12.5 ng Halo–PLCδ-PH (volumes denote per well) were transfected into βarr1/2-deficient HEK293A cells in a six-well plate. After incubation for 1 day, cells were harvested, suspended in 1 ml of the assay buffer, dispensed in a 96-well white plate at a volume of 45 µl per well and mixed with 50 µl of a buffer consisting of 800 nM HiBiT–TMR and 20 µM furimazine (ABAMA Chemicals) in the assay buffer. After 40-min incubation at room temperature, the plate was measured for baseline luminescence. Then, 5 µl of 20× ligands serially diluted in the assay buffer were manually added. The plate was immediately read at room temperature for the following 15 min at a measurement interval of 40 s. For each well, the luminescent counts over the recorded time were first normalized to the initial

measurement. Then, for each time point, the values in ligand stimulated conditions were further normalized to that in vehicle conditions. The vehicle-normalized luminescent signals from 13 min to 15 min after ligand addition were averaged and used to denote endpoint endocytosis response.

Western blot

HEK293A cells were transfected with the SmBiT–βarr and LgBiT–CAAX constructs by following the procedure described in the NanoBiT βarr recruitment assay. After 1-day culture, the transfected cells were lysed by SDS–PAGE sample buffer (62.5 mM Tris-HCl pH 6.8, 50 mM dithiothreitol, 2% SDS, 10% glycerol and 4 M urea) containing 1 mM EDTA, 1 mM phenylmethylsulfonyl fluoride and 2 mM sodium orthovanadate. Lysates derived from an equal number of cells were separated by 8% or 12.5% SDS–PAGE. Subsequently, the proteins were transferred to a nitrocellulose membrane (GE Healthcare). The blotted membrane was blocked with 5% skim milk-containing blotting buffer (10 mM Tris-HCl pH 7.4, 190 mM NaCl and 0.05% Tween-20), immunoblot with primary (1 µg ml⁻¹, unless otherwise indicated) and secondary antibodies (1:2,000 dilution). Primary antibodies used in this study were anti-α-tubulin antibody (mouse monoclonal, clone DM1A; Santa Cruz Biotechnologies, sc-32293; 1:2,000 dilution), anti-βarr1 (Cell Signaling Technology, 12697, D8O3J, lot 1; 1:1,000 dilution) and anti-βarr2 (rabbit monoclonal; CST, 3857, C16D9). Secondary antibodies that were conjugated with horseradish peroxidase were anti-mouse IgG (GE Healthcare, NA9310) and anti-rabbit IgG (GE Healthcare, NA9340). Membranes were soaked with a luminol reagent (100 mM Tris-HCl pH 8.5, 50 mg ml⁻¹ Luminol Sodium Salt HG (FujiFilm Wako Pure Chemical), 0.2 mM *p*-coumaric acid and 0.03% (v/v) of H₂O₂). A chemiluminescence image was acquired and band intensity was analyzed with Amersham Imager 680 (Cytiva). The intensities of individual bands were quantified with NIH ImageJ.

Single-molecule imaging

Single-molecule imaging analysis was performed as described previously with modifications[8,23,24]. A plasmid mixture of 100 ng of LgBiT–V2R, 50 ng of EGFP–βarr2 (WT, C-3Q and NC-4Q) and 25 ng of Halo–PLCδ-PH were transfected into βarr1/2-deficient HEK293 cells in a 6-cm dish with two coverslips (Matsunami, 25 mm, No.1) by Lipofectamine 3000 on the day before imaging. For CCS visualization, cells were transfected with 100 ng of LgBiT–V2R, 200 ng of untagged βarr2 WT, 25 ng of Halo–PLCδ-PH and 50 ng of EGFP–CLC under the same conditions. The LgBiT and HaloTag were labeled for 15 min at 37 °C by 1 nM SF650–FiBiT peptide and 300 pM Janelia Fluor 549 (JF549) HaloTag ligand, respectively. After a 5-min wash with 3 ml of 10% FBS FluoroBrite DMEM (Thermo Fisher Scientific) three times, the cells on a coverslip were mounted on the Attofluor cell chamber. After washing with 400 µl of 0.01% BSA–HBSS three times, cells were incubated for 15 min at room temperature in 400 µl of 0.01% BSA–HBSS. The functionality of LgBiT–V2R in the βarr-dependent endocytosis was previously confirmed by flow cytometry and a HiBiT-based receptor internalization assay[23].

Single-molecule imaging was performed using a homemade quad-color TIRF microscope system with a 488-nm, 30-mW laser (OBIS 488, Coherent) for EGFP, with a 561-nm, 50-mW laser (OBIS 561, Coherent) for JF549 and with a 637-nm, 100-mW laser (OBIS 637, Coherent) for SF650 through the objective (PlanApo ×100, numerical aperture 1.49; Nikon) by a dichroic mirror (ZT405/488/561/640/705rpc, Chroma). Fluorescence images were spectrally split into four channels using image-splitting optics with two W-view Gemini (Hamamatsu, A12801-01) connected in tandem to a W-view Gemini-2C (Hamamatsu, A12801-10) and captured simultaneously by two scientific complementary metal–oxide–semiconductor cameras (ORCA Fusion BT; Hamamatsu, C15440-20UP). In the image-splitting optics, dichroic mirrors (FF640-FDi01, Semrock, in W-view Gemini-2C and T720lpxr-UF1,

Chroma, in a W-view Gemini for long wavelength; T560lpxr-UF21, Chroma for short wavelength) and emission filters (ET685/50m and ET670/50m, Chroma for SF650, FF01-600/52-25, Semrock for JF549 and ET525/50 m, Chroma for EGFP) were included to split images (512 × 512 pixels, pixel size: 65 nm per pixel). The TIRF microscope system was controlled by AIS (version 2.5.79), Zido (https://eng.zido.co.jp/). We took 300-frame videos (33 fps) repeatedly recorded at the same cell positions at 5-min intervals for 15 min (four time points). Then, 100 µl of ligand solution (1 µM AVP at final concentration) in 0.01% BSA–HBSS was added into the chamber 30 s before the second time point of the time-lapse imaging.

As previously described in detail[23], we conducted simultaneous three-color single-molecule imaging to enable precise quantification of dynamics and colocalization without temporal offsets. The excitation laser powers at the specimen were carefully optimized: 0.5 µW µm⁻² for the 488-nm laser and 1 µW µm⁻² for the 561-nm and 637-nm lasers. The lower power for the EGFP channel specifically addresses potential bleedthrough concerns. To exclude the possibility of fluorophore misidentification because of spectral overlap, we evaluated bleedthrough across the three detection channels. We confirmed that the bleedthrough signals were as low as background levels, ensuring that it did not affect the single-molecule-tracking analysis (Extended Data Fig. 9a,b).

Single-molecule tracking analysis

Processing of multiple TIFF files (16-bit; subtract background with 25-pixel rolling ball radius) was performed using ImageJ with a batch-processing macro (https://github.com/masataka-yanagawa/ImageJ-macro-ImageProcessingSMT). The alignment between the two channels based on the images of multicolor beads (TetraSpeck microspheres; Thermo Fisher Scientific, T7279) was performed using AAS (version 2.6.9), Zido (https://eng.zido.co.jp/). The single-molecule tracking analysis was performed using AAS with the following parameters: detection mode, Gauss fit scanning; ROI, 12 pixels; interval, 3 pixels; intensity threshold, 15, 12 and 10 a.u. for GFP, JF549 and SF650, respectively; maximum connection frame, 2 frames; maximum connection length, 8 pixels; minimum number of frames per trajectory, 12 frames; connection mode, nearest neighbor. Two spots are connected as a trajectory of a single molecule when detected in successive frames within 8 pixels (520 nm) and within the two frames. Given that the VB-HMM analysis requires trajectory lengths of at least 12 frames, the analysis did not include information from shorter trajectories.

For VB-HMM analysis, we followed the established methodology detailed in Yanagawa et al.[8], which uses basically same algorithm as vbSPT (version 1.1.4)[42]. The original vbSPT source code is publicly available online (https://vbspt.sourceforge.net/). The AAS software enables rapid single-molecule tracking analysis and VB-HMM analysis on a single platform. The VB-HMM method assumes one to five diffusion state models with distinct diffusion coefficients (D_1 to D_5), where molecules transition between states according to Markov process dynamics with a transition matrix A. State assignments are determined using the VB-EM algorithm based on step-size time series, with the optimal number of states selected using VB lower bounds (Extended Data Fig. 9g). The hyperparameters that set the initial distributions of the parameters of the observation probability used in this study were carefully selected on the basis of previous research. The values were set as follows: n_tilde, 1; c_tilde, 0.001; w_pi_tilde, 1; b_tilde, 0.01; mag, 30.

All subsequent analyses (trajectory analysis, diffusion dynamics, density measurements, intensity distribution analysis, colocalization analysis and statistical analysis) were performed using smDynamicsAnalyzer (smDA, https://github.com/masataka-yanagawa/IgorPro8-smDynamicsAnalyzer), a custom-built program based on Igor Pro. A detailed description of smDA was provided in our previous study[9].

The MSD was calculated for each trajectory using the following equation:

$$\mathrm{MSD}\,(n\Delta t) = \frac{1}{N-1-n} \sum_{j=1}^{N-1-n} \left[\{x(j\Delta t + n\Delta t) - x(j\Delta t)\}^2 \right.$$
$$\left. + \{y(j\Delta t + n\Delta t) - y(j\Delta t)\}^2 \right]$$

where n is the frame length, Δt is the frame rate (30.5 ms) and N is the total number of frames in the trajectory. The MSD versus Δt plot was fitted using the equation:

$$\mathrm{MSD}\,(\Delta t) = \frac{L^2}{3} \left(1 - \exp \exp \left(\frac{-12D\Delta t}{L^2} \right) \right) + 4\varepsilon^2$$

where L is the confinement length and D is the diffusion coefficient as Δt approaches 0. The VB-HMM analysis classifies diffusion states on the basis of frame-to-frame step-size changes in molecular trajectories, rather than using predefined confinement lengths. The subsequent analysis using MSD versus Δt plots of the classified trajectories provides information of the time evolution of each diffusion state.

The particle density was estimated as the plateau value of the mean local density function (Extended Data Fig. 9c, red line)[28]. The mean local density function is defined as follows:

$$d_{\mathrm{avg}}(r) = \frac{1}{n} \sum_{i=1}^{n} \frac{N_{Pi}(r)}{\pi r^2}$$

where n is the number of particles within the frame and $N_{Pi}(r)$ is the number of particles N within a distance r of particle i. For distances less than that to the nearest adjacent particle, we can define $d_{\mathrm{avg}}(r) = 1/r^2$. As r increases, the mean local density approaches the mean particle density in the cell, reaching a plateau before converging to 0 because of cell boundaries. To estimate the mean particle density, we identify the plateau value in the mean local density function using its first-order difference (Extended Data Fig. 9c, blue line). The apparent cell area (S) was estimated as the number of particles per density[43] The estimated density and cell area are averaged across all analyzed frames and used as representative values for the cell in subsequent comparative analyses. This method provides an automated and reproducible way to estimate spot density and cell area, comparable to manual analysis techniques (Extended Data Fig. 9d,e). In the intensity–density histogram analysis, the histogram displays the product of the probability density distribution of the particle intensity and the calculated particle density as a heat map[23].

The colocalization of two particles is detected if the two particles are within 100 nm in the same frame. The positional accuracy of each localization was estimated as 25 nm for GFP, 20 nm for JF549 and 20 nm for SF650 according to the formula[43]:

$$\mathrm{Var}(\mu) = \frac{\sigma_a^2}{N} \left(\frac{16}{9} + \frac{8\pi\sigma_a^2 b^2}{Na^2} \right)$$

where $\mathrm{Var}(\mu)$ is the variance of the center coordinates of the fluorophore in the xy plane, σ_a is the standard deviation of the two-dimensional Gaussian fitting function with a correction for pixel size a (65 nm per pixel in this study), and b^2 is the estimated background photon count per pixel. The threshold value of 100 nm used in the current colocalization analysis corresponds to ~3 s.d., which is high enough to avoid false-negative determinations. The higher threshold increases the false discovery rate, but ~3 s.d. is required for convincing on-time estimation considering frame-by-frame colocalization detection over 20 frames. The diffusion state step count quantifies the total number of time steps during which molecules occupy specific diffusion states while colocalized. When two molecules colocalize, we count the number of time steps for each diffusion state throughout their colocalization

period. The CI between molecules A and B in the cell area S was calculated as follows: CI = $([A\cdot B])/([A][B])$, where $[A\cdot B]$ = (the number of the colocalized steps)/S, $[A]_{\mathrm{tot}}$ = (the diffusion state step count of A)/S, $[B]_{\mathrm{tot}}$ = (the diffusion state step count of B)/S, $[A]$ = $[A]_{\mathrm{tot}} - [A\cdot B]$ and $[B]$ = $[B]_{\mathrm{tot}} - [A\cdot B]$. Changes in the fractions or colocalization steps in the diffusion states were the differences before and 15 min after stimulation of the same cell. The on-event rate was calculated as the initial slope of the cumulative event number divided by S[24].

Statistical analyses
Statistical analyses were performed using GraphPad Prism 10 (GraphPad) and the methods are described in the figure legends. The representation of symbols and error bars is described in the legends. Symbols are either the mean values of indicated numbers of independent experiments or numbers of measured cells from two experiments. Unless otherwise noted, error bars and shaded areas denote the s.e.m. For multiple-comparison analysis, a two-way analysis of variance (ANOVA) followed by Dunnett's test or Tukey's test or the multiple t-test was used. Further details of the statistical tests, P values and test statistics are provided in the Source Data.

Reporting summary
Further information on research design is available in the Nature Portfolio Reporting Summary linked to this article.

Data availability
All data generated or analyzed during this study are available within the article and Supplementary Information. Structural data used in this study are available from the PDB under accession codes 5TV1, 6U1N and 7KH0. The ImageJ macro used for image preprocessing is available from GitHub (https://github.com/masataka-yanagawa/ImageJ-macro-ImageProcessingSMT) and the vbSPT algorithm is available online (https://vbspt.sourceforge.net/). AAS software is available online (https://eng.zido.co.jp/). Simulation input files were deposited to Zenodo (https://doi.org/10.5281/zenodo.15549775)[44]. Source data are provided with this paper.

References
37. Shihoya, W. et al. Crystal structures of human ETB receptor provide mechanistic insight into receptor activation and partial activation. *Nat. Commun.* **9**, 4711 (2018).
38. Shukla, A. K. et al. Structure of active β-arrestin1 bound to a G protein-coupled receptor phosphopeptide. *Nature* **497**, 137 (2013).
39. Itoh, T., Hasegawa, J., Tsujita, K., Kanaho, Y. & Takenawa, T. The tyrosine kinase Fer is a downstream target of the PLD–PA pathway that regulates cell migration. *Sci. Signal* **2**, ra52 (2009).
40. Abe, M. et al. PMP2/FABP8 induces PI(4,5)P$_2$-dependent transbilayer reorganization of sphingomyelin in the plasma membrane. *Cell Rep.* **37**, 109935 (2021).
41. Grundmann, M. et al. Lack of β-arrestin signaling in the absence of active G proteins. *Nat. Commun.* **9**, 341 (2018).
42. Persson, F., Lindén, M., Unoson, C. & Elf, J. Extracting intracellular diffusive states and transition rates from single-molecule tracking data. *Nat. Methods* **10**, 265–269 (2013).
43. Mortensen, K. I., Churchman, L. S., Spudich, J. A. & Flyvbjerg, H. Optimized localization-analysis for single-molecule tracking and super-resolution microscopy. *Nat. Methods* **7**, 377 (2010).
44. Kuramoto, R. Membrane-domain compartmentalization of active GPCRs by β-arrestins via PIP$_2$ binding. *Zenodo* https://doi.org/10.5281/zenodo.15549775 (2025).

Acknowledgements

Author contributions

Competing interests

The authors declare no competing interests.

Additional information

Extended data is available for this paper at https://doi.org/10.1038/s41589-025-01967-4.

Supplementary information The online version contains supplementary material available at https://doi.org/10.1038/s41589-025-01967-4.

Correspondence and requests for materials should be addressed to Asuka Inoue.

Peer review information *Nature Chemical Biology* thanks Jana Selent and the other, anonymous reviewer(s) for their contribution to the peer review of this work.

Reprints and permissions information is available at www.nature.com/reprints.

a NTSR1-βarr1 (PDBID : 6UP7)


b
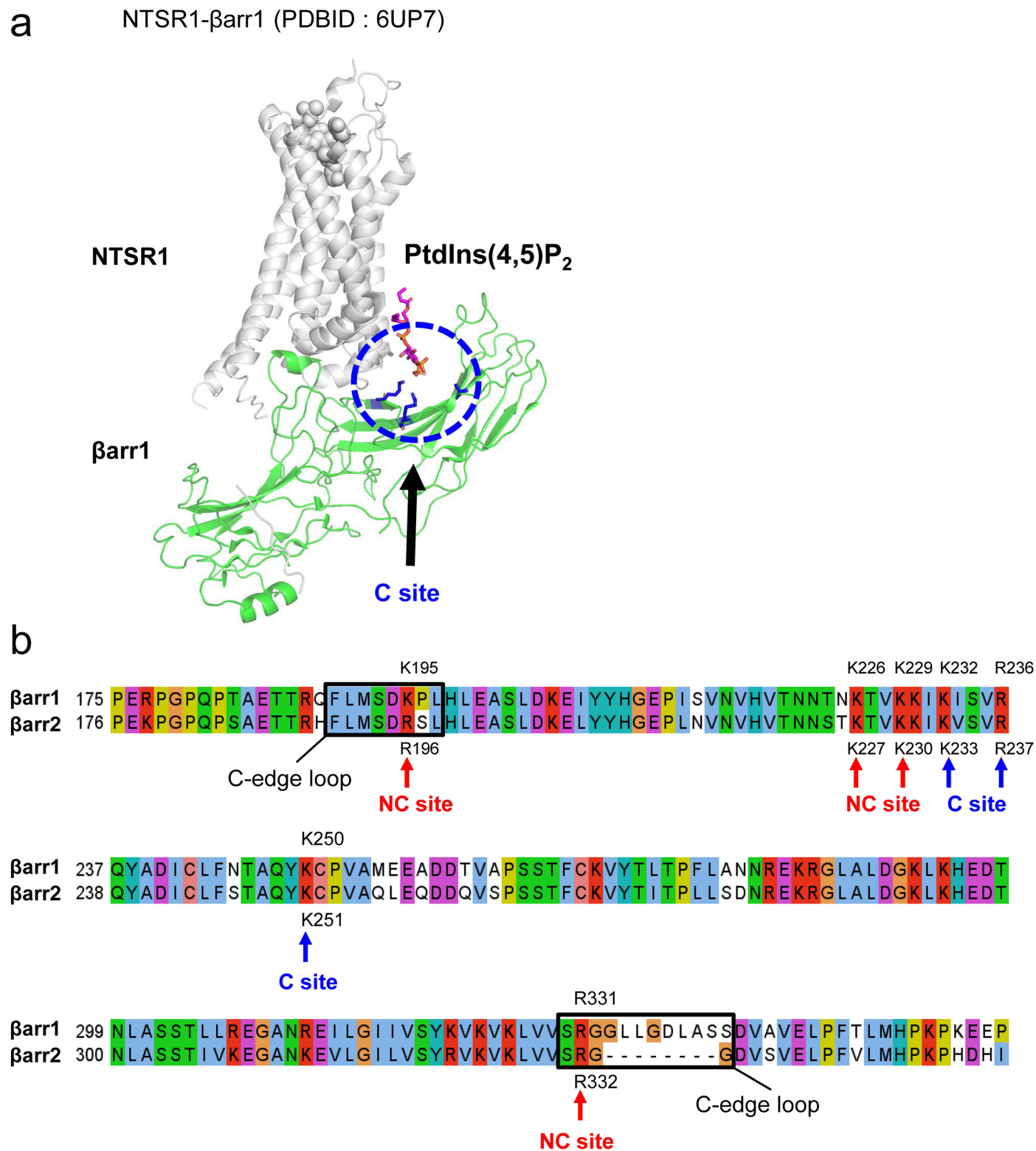
Extended Data Fig. 1 | Positions of PtdIns(4,5)P₂-binding sites. (a) Structure of βarr1 in complex with NTSR1 and one PtdIns(4,5)P₂ molecule in a detergent micelle (PDB ID: 6UP7). **(b)** Sequence alignments of the C domain from the human βarr1 and βarr2. Positive charge r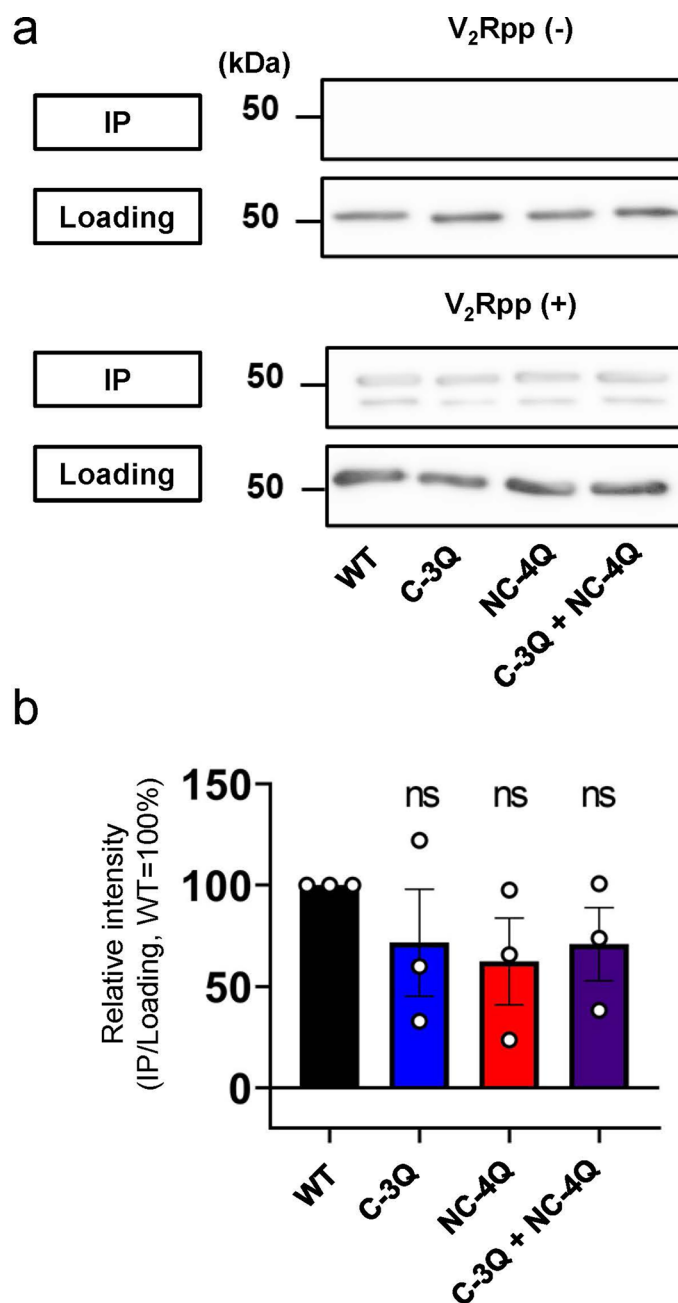esidues are shown in red, negative charge residues in magenta, hydrophobic residues in blue, polar residues in green, aromatic residues in cyan, cysteines in pink, glycines in orange, proline in yellow, and non-conserved residues in white. The red arrow points to the NC site, and the blue arrow points to the C site.
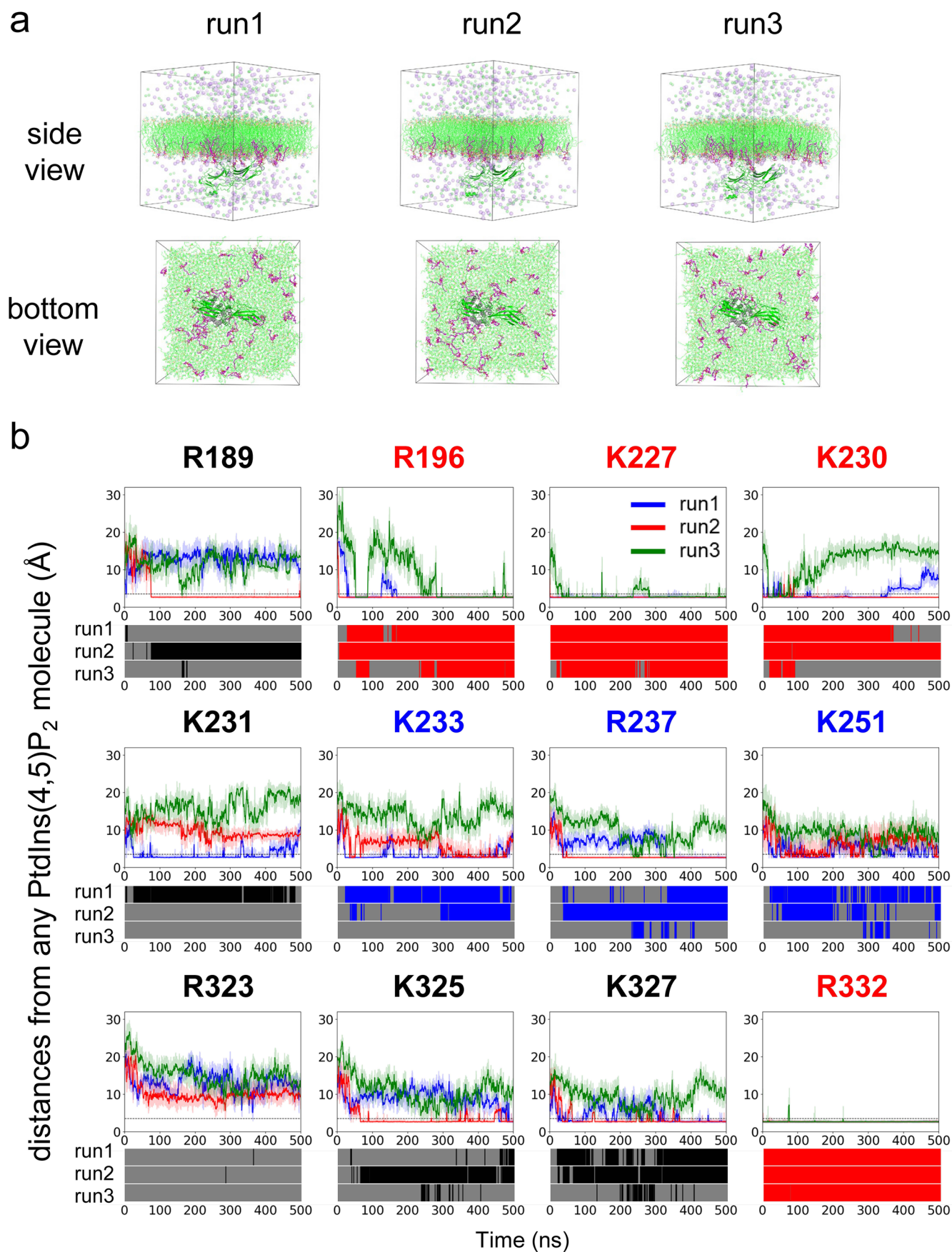
Extended Data Fig. 2 | See next page for caption.

Extended Data Fig. 2 | Distance analyses for PtdIns(4,5)P$_2$ molecules in every positively charged residue during MD simulations. (a) Initial coordinates for three independent simulations with randomly placed PtdIns(4,5)P$_2$. The V2RΔC– βarr2 complex was embedded in POPC membrane containing PtdIns(4,5)P$_2$ in a 16 × 16 × 16 nm^3 box and this system was solvated and neutralized to a concentration of 150 mM NaCl. **(b)** (top) Distance trajectories of βarr2 between the basic residues in the C domain and the PtdIns(4,5)P$_2$ from 3 independent MD simulations. Runs 1, 2 and 3 are colored in blue, red and green, respectively. (bottom) Frames with distances of ≤3.5 Å are shown in black, while frames with distances >3.5 Å are shown in gray. For residues in the NC site, frames with distances of ≤3.5 Å are highlighted in red. For residues in the C site, frames with distances of ≤3.5 Å are highlighted in blue.

a

V$_2$Rpp (-)

| IP | 50 |
| Loading | 50 |

V$_2$Rpp (+)

| IP | 50 |
| Loading | 50 |

WT   C-3Q   NC-4Q   C-3Q + NC-4Q

b

Extended Data Fig. 3 | βarr conformational changes by V2R phsphopeptide using Fab30. (**a**) Representative western blot imaging for the co-immunoprecipitation analysis. The indicated βarr protein constructs were subjected to the Fab30 pull-down assay in presence of the V2Rpp phosphopeptide. (**b**) Quantification of the data in (**a**). Bars and error bars represent mean and SEM, respectively, of three independent experiments. For the statistical analyses, data were analyzed by one-way ANOVA followed by the Dunnett's test for multiple comparison analysis. ***$P < 0.001$ vs. WT.
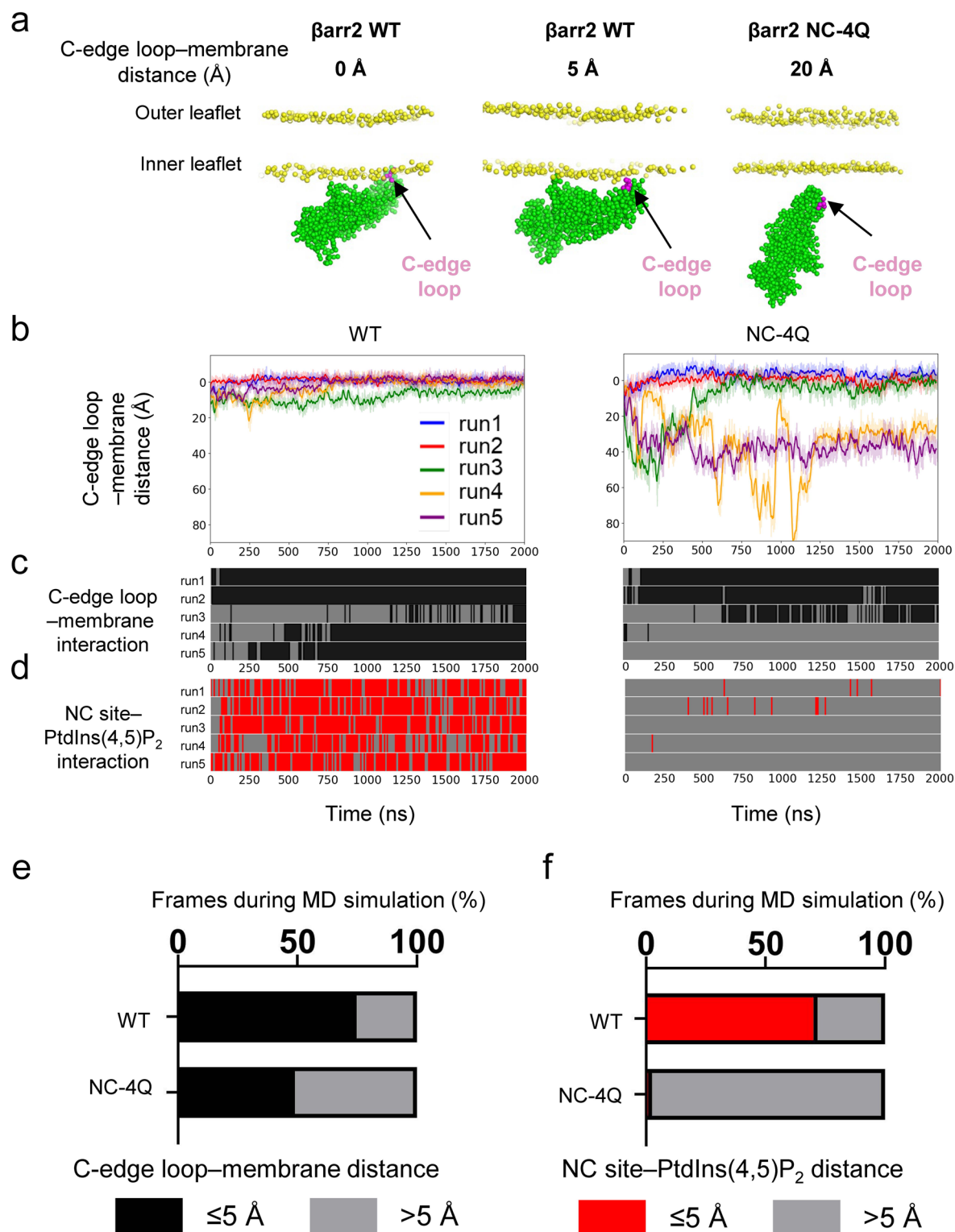
Extended Data Fig. 4 | Analysis of C-edge loop membrane interaction and PtdIns(4,5)P$_2$ binding at the NC site during CG simulation. (**a**) Snapshots of the C-edge loop and membrane distances at 0 Å, 5 Å and 20 Å in the CG MD simulations of βarr2 WT or NC-4Q. Snapshots are representative of five independent CG MD simulations that yielded similar results. (**b**) Distance trajectories of βarr2 WT and NC-4Q between the basic residues in the C-edge loop and the membrane from five independent CG MD simulations. (**c**) Frames with C-edge loop–membrane distances of ≤5 Å (membrane association) and >5 Å

are shown in black and gray, respectively. (**d**) Frames with NC site–PtdIns(4,5)P$_2$ interaction (as defined by 2 or more NC residues being within 5 Å distance from PtdIns(4,5)P$_2$) are shown in red, while frames with the other NC site–PtdIns(4,5)P$_2$ distances are shown in gray. In both (**c**) and (**d**), colors represent every 10-ns time intervals and distinguish between the interaction period (≤5 Å) and the non-interaction period (>5Å). (**e, f**) Total frames from the runs 1–5 where the C-edge loop interacted with the membrane (**e**) and the NC site interacted with PtdIns(4,5)P$_2$, calculated by assessing interactions at 100-ps intervals.
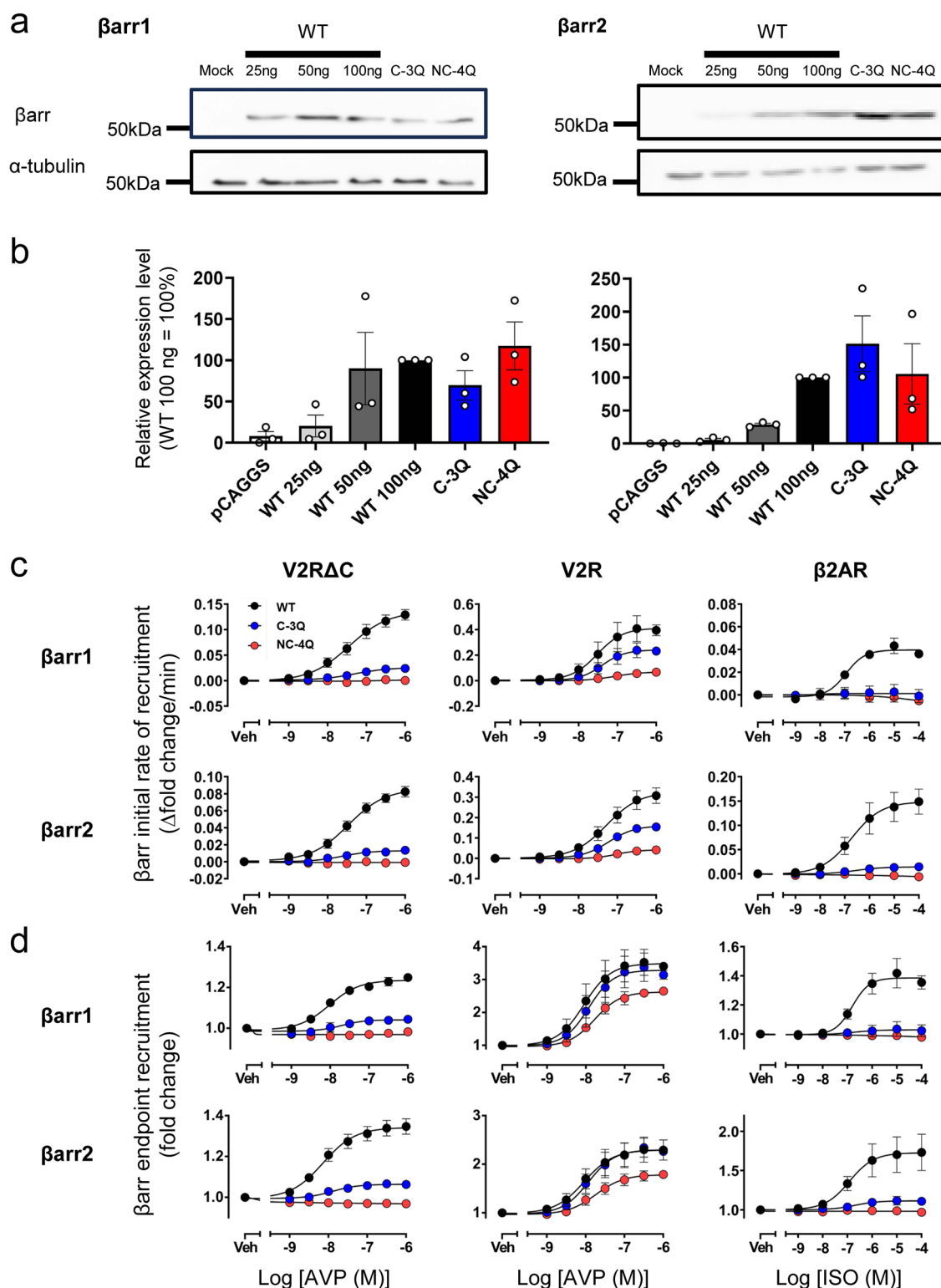
Extended Data Fig. 5 | GPCR-induced βarr recruitment for the NC-site βarr mutant. (a) Western blot analyses of βarr mutants (WT, C-3Q and NC-4Q). The N-terminally SmBiT-fused βarr constructs were expressed in ΔβarrΓ/2 HEK293 cells. **(b)** Densiometric quantification of the western blot analyses. Band intensity of βarr was normalized by that of α-tubulin. For the individual experiments, the βarr/α-tubulin ratios were further normalized to that in WT βarr. Symbols and error bars represent mean and SEM, respectively, 3 independent experiments with each performed in duplicate. **(c, d)** Concentration-response curves illustrate the change in the initial rate of recruitment **(c)** and the endpoint of recruitment **(d)** for WT, C-3Q and NC-4Q for both βarr1 and βarr2 in the V2RΔC, V2R and β2AR. Symbols and error bars represent mean and SEM, respectively, 3 independent experiments with each performed in duplicate.
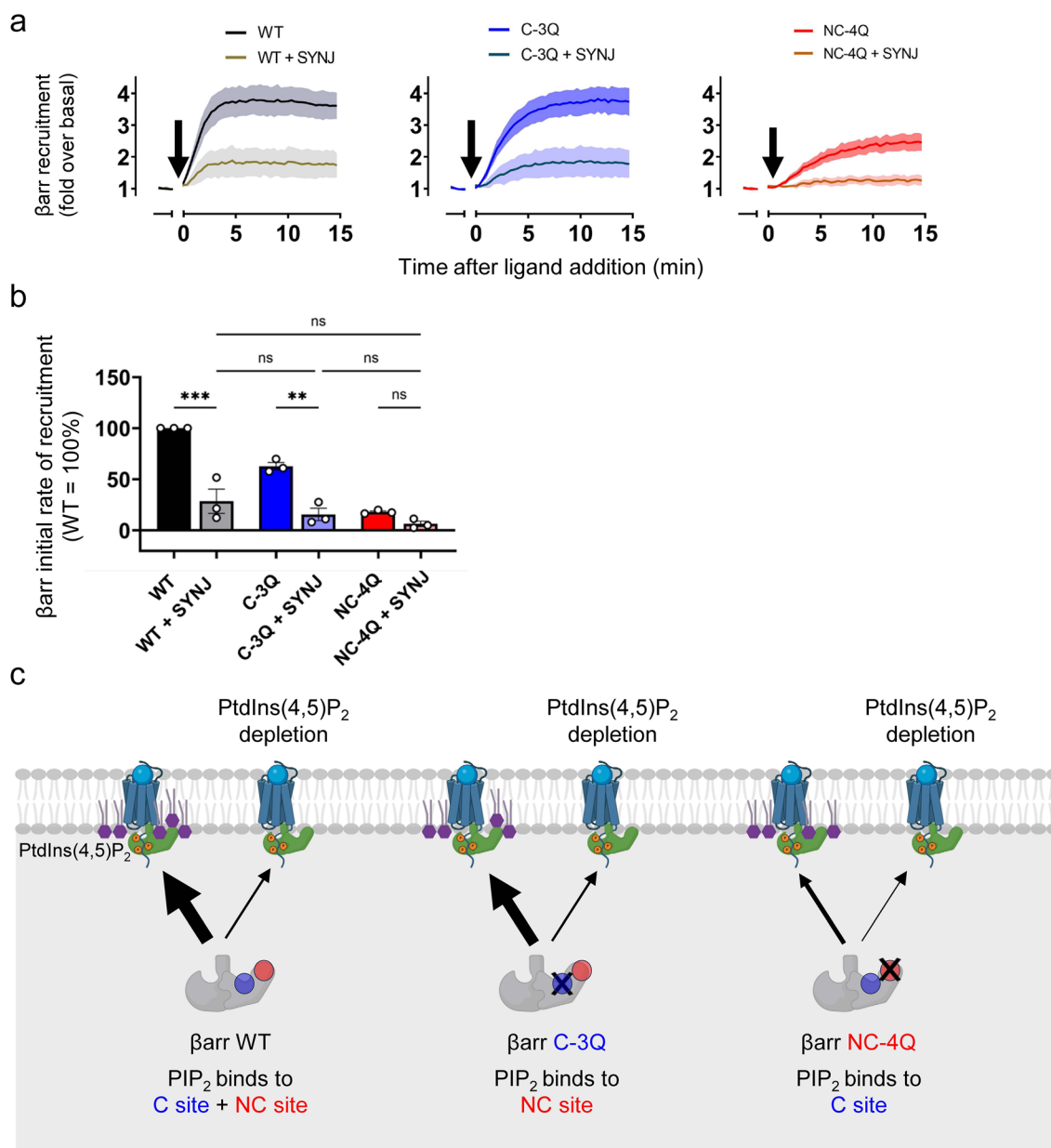
Extended Data Fig. 6 | V2R-induced βarr2 recruitment under PtdIns(4,5)P₂-depleted conditions. (**a**) Luminescent kinetics of the βarr2 recruitment responses upon V2R ligand stimulation under conditions with or without SYNJ overexpression. Luminescence was measured over time after 1 µM AVP (at t = 0 min), and values are shown as fold change (FC) over basal luminescent signals. Data represent the mean of three independent biological replicates, each measured in technical duplicate (n = 3). Shaded regions denote SEM (n = 3). WT, C-3Q, and NC-4Q are colored in black, blue, and red, respectively, with higher transparency applied under SYNJ overexpression conditions. (**b**) Quantification of the NanoBiT assay. Bar graph showing the initial rate of recruitment for WT, C-3Q and NC-4Q for βarr2 with or without SYNJ. (**c**) Proposed model of βarr recruitment via PtdIns(4,5)P₂-binding sites under PtdIns(4,5)P₂-depleted conditions. WT binds PtdIns(4,5)P₂ via both C and NC sites and shows reduced membrane recruitment when PtdIns(4,5)P₂ is depleted. C-3Q, which retains the NC site, also shows reduced recruitment, indicating that both sites contribute to PtdIns(4,5)P₂-dependent binding. NC-4Q, binding only via the C site, fails to recruit even without depletion, suggesting that the NC site is essential under low PtdIns(4,5)P₂ levels. For each experiment, data were normalized to WT response performed in parallel. Bars and error bars are mean and SEM, respectively, of three independent experiments with each performed duplicate. For the statistical analyses, data were analyzed by two-way ANOVA followed by the Tukey's test for multiple comparison analysis. ns, not significantly different between the groups. *P < 0.05, **P < 0.01 and ***P < 0.001. Schematic created with BioRender.com.
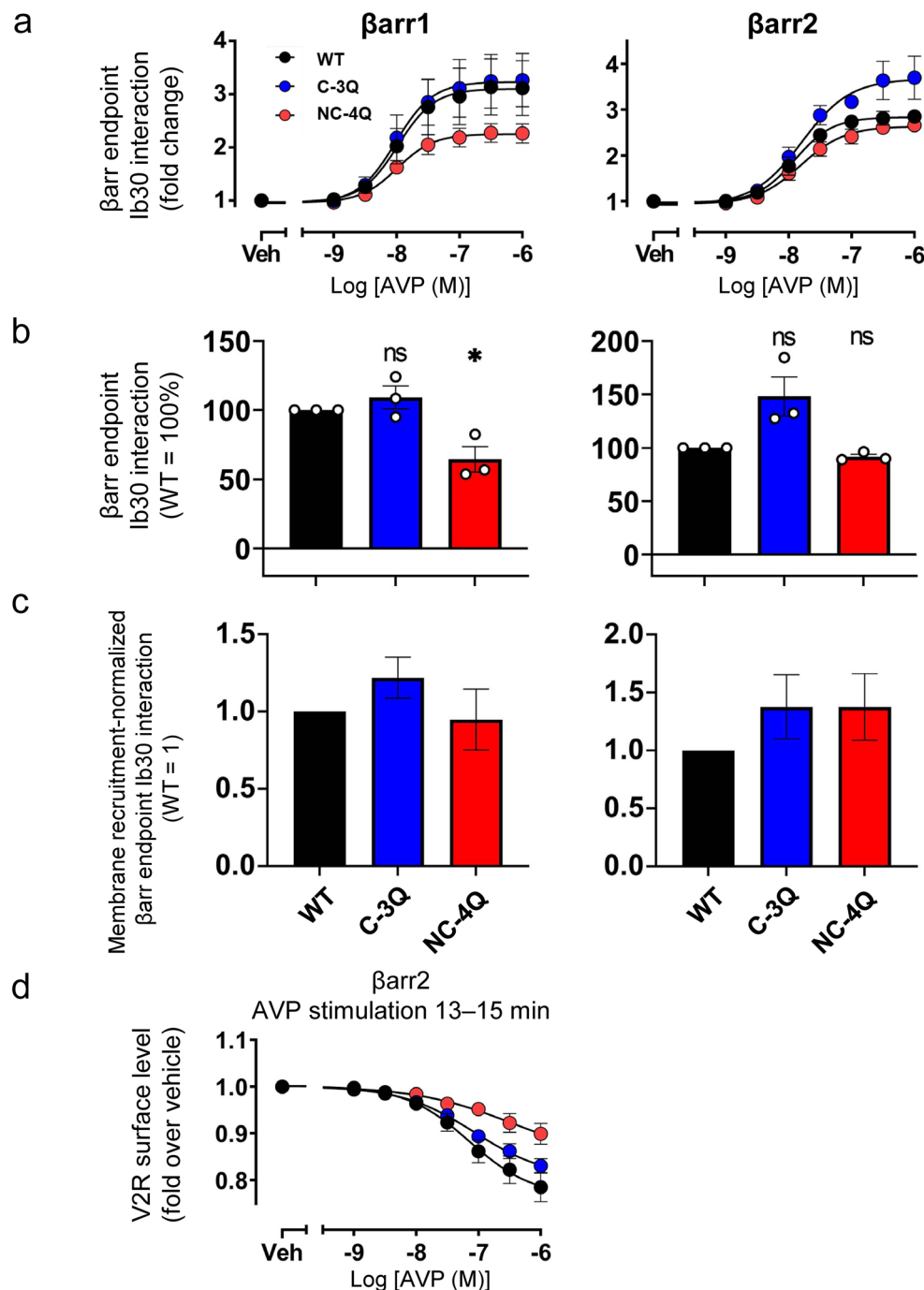
Extended Data Fig. 7 | GPCR-induced βarr conformational change for the NC-site βarr mutant. (**a**) Concentration-response curves illustrate the change in the endpoint of Ib30 interaction for WT, C-3Q and NC-4Q for both βarr1 and βarr2 in the V2R. Symbols and error bars represent mean and SEM, respectively, 3 independent experiments with each performed in duplicate. (**b**) Normalized efficacy of endpoint of Ib30 interaction. For each experiment, these data were normalized to WT response. (**c**) Normalization of the Ib30 assay to the level of membrane recruitment. For each experiment, data were normalized to WT response. Bars and error bars are mean and SEM, respectively, of three independent experiments with each performed duplicate. (**d**) Concentration-response curves of the HiBiT-based V2R internalization assay. HiBiT-V2R and EGFP-βarr2 (WT, C-3Q or NC-4Q) were co-expressed in Δβarr1/2 HEK293 cells and AVP-induced HiBiT-V2R internalization was monitored. Symbols and error bars represent mean and SEM, respectively, three independent experiments with each performed in duplicate. For the statistical analyses, data were analyzed by one-way ANOVA followed by the Dunnett's test for multiple comparison analysis. ns, not significantly different between the groups. *$P < 0.05$ vs. WT.
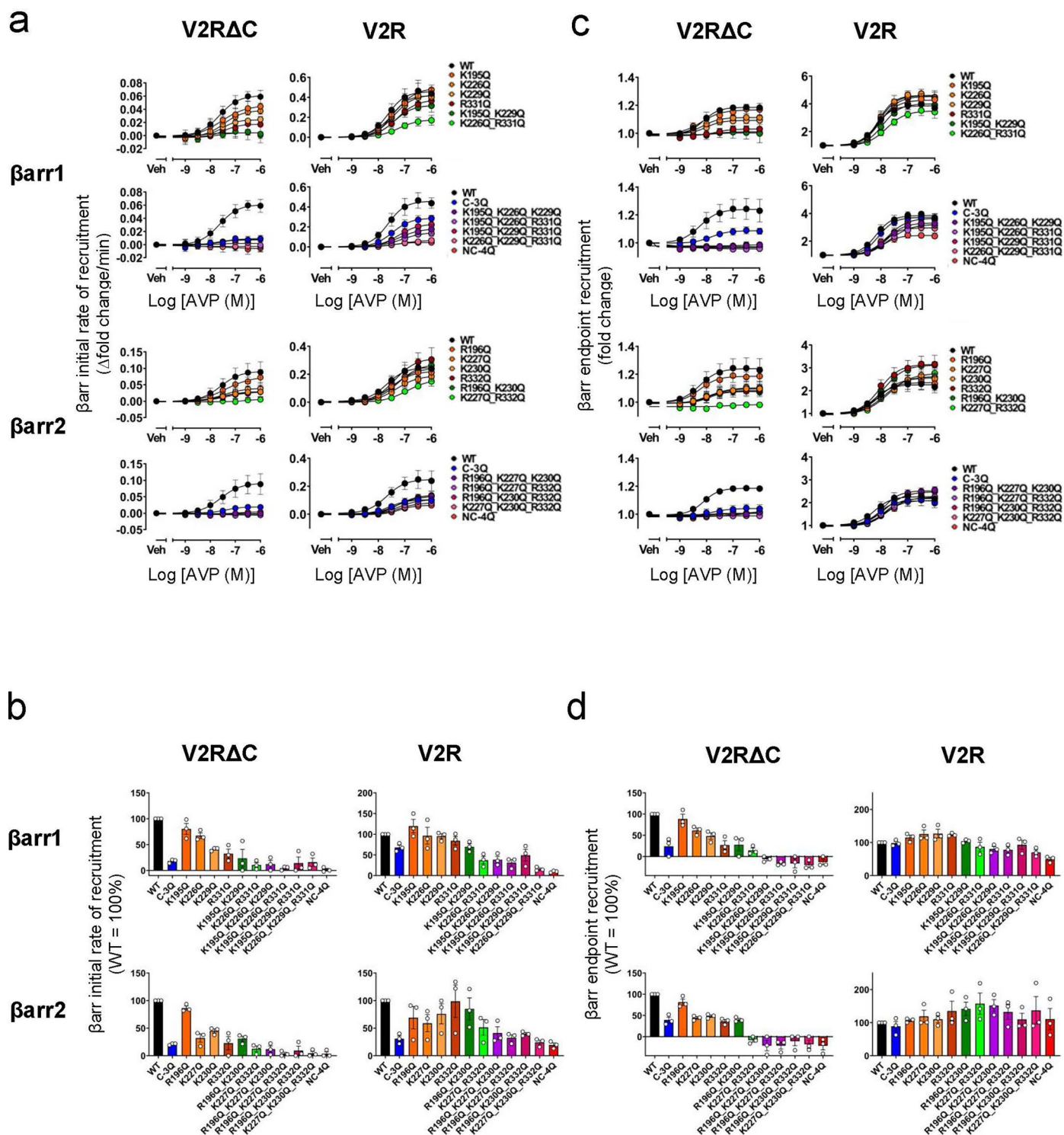
Extended Data Fig. 8 | Effects of GPCR-induced βarr recruitment by single and combined mutations at the NC site. (**a**) Concentration-response curves illustrate the change in the initial rate of recruitment for WT, C-3Q and NC site single, double, and triple βarr mutants for both βarr1 and βarr2. (**b**) Normalized efficacy of initial rate of recruitment. For each experiment, these data were normalized to WT response. (**c**) Concentration-response curves illustrate the endpoint of recruitment for WT, C-3Q and NC site single, double, and triple

βarr mutants for each βarr1 and βarr2. (**d**) Normalized efficacy of endpoint of recruitment. For each experiment, these data were normalized to WT response. For Extended Data Fig. 8a, c, Symbols and error bars represent mean and SEM, respectively, 3 independent experiments with each performed in duplicate. For Extended Data Fig. 8b, d, Bars and error bars are mean and SEM, respectively, of three independent experiments with each performed duplicate.
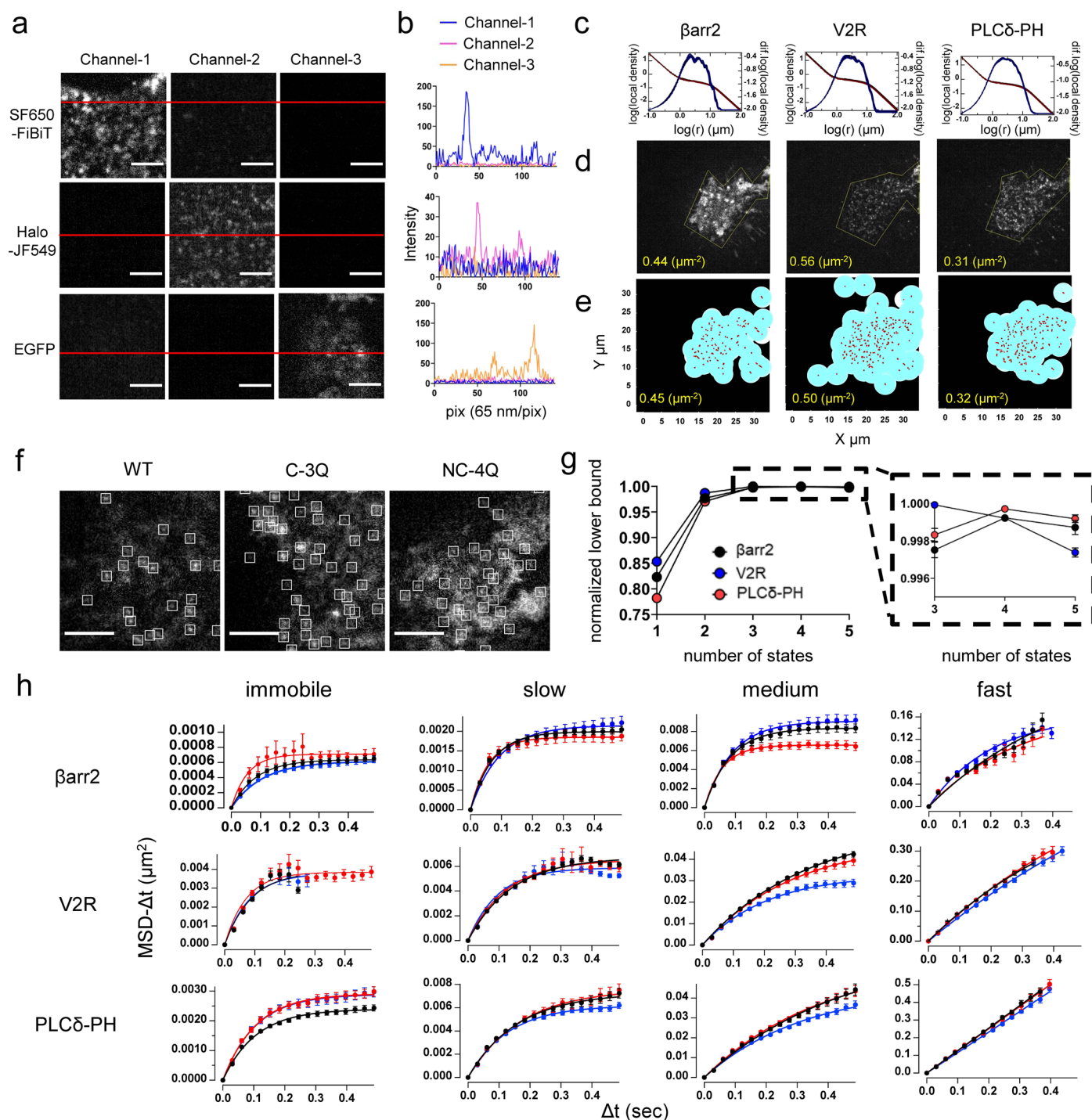
Extended Data Fig. 9 | Single-molecule behaviors of V2R, βarr and PLCδ-PH.
(**a**) Images of cells expressing LgBiT-V2R (SF650-FiBiT labeling) and, Halo-PLCδ-PH (labeled with SF650-FiBiT and Halo-JF549 labeling), respectively, and EGFP-βarr2 measured across three channels. (**b**) The intensity profile along the red line for each channel. Scale bar: 3 μm (**c**) The mean local density (red, left axis) and its first-order difference (blue, right axis) were plotted versus log(r), where r is the radius of the circle around each particle to calculate the local density. (**d, e**) Comparison of the mean densities estimated by hand (**d**) and by the local density analysis algorithm (**e**). Yellow lines in the upper panels were drawn by hand. The densities in the upper panels (yellow characters) were calculated as spot number/area of a frame. The densities in the lower panels were estimated by the mean local density analysis of the same frame. (**f**) Representative TIRF

microscopic image of EGFP-βarr2 (βarr2-WT, C-3Q, or NC-4Q) at the before AVP stimulation (basal). The bright spots of tracked βarr2 are surrounded by white lines. Scale bar: 3 μm. (**g**) Numbers of HMM states and its selection. Single-molecule-tracking data for βarr2 (black), V2R (blue) and PLCδ-PH (red) molecules were classified based on the one- to five-state HMMs. Note that the four-state model, although the differences among the three to five states were modest, gave the top score for the lower bound values. (**h**) MSD-Δt plots of βarr2, V2R and PLCδ-PH after 15 min AVP stimulations under the βarr2 WT (black)-, C-3Q (blue)-, or NC-4Q (red)-expressing conditions. WT (n = 36), C-3Q (n = 32), NC-4Q (n = 23); n represents individual cells analyzed across two independent biological replicates. In Extended Data Fig. 9g, h, bars and error bars represent mean and SEM, respectively.
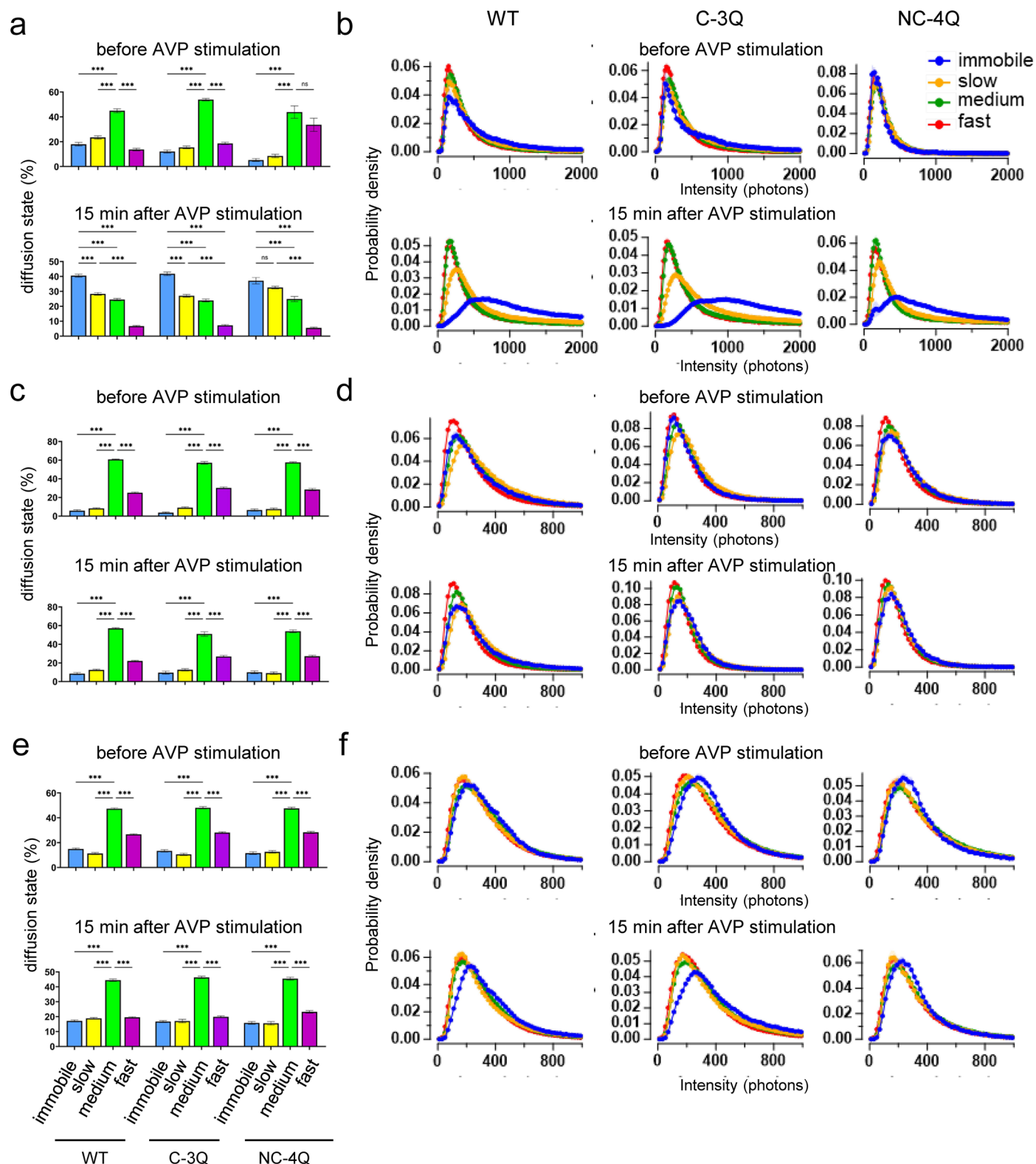
Extended Data Fig. 10 | Single-molecule behaviors of V2R, βarr and PLCδ-PH.
(**a**, **b**) The diffusion state (**a**) and Normalized intensity distribution histograms
(**b**) for each diffusion state of βarr2 WT, C-3Q and NC-4Q at the before AVP
stimulation, after 15 min AVP stimulation. (**c**, **d**) The diffusion state (**a**) and
Normalized intensity distribution histograms (**b**) for each diffusion state of
PLCδ-PH co-expressing EGFP-βarr2 WT, C-3Q and NC-4Q at the before AVP
stimulation, after 15 min AVP stimulation. (**e**, **f**) The diffusion state (**a**) and

Normalized intensity distribution histograms (**b**) for each diffusion state of V2R
co-expressing EGFP-βarr2 WT, C-3Q and NC-4Q at the before AVP stimulation,
after 15 min AVP stimulation. WT ($n = 36$), C-3Q ($n = 32$), NC-4Q ($n = 23$); n
represents individual cells analyzed across two independent biological
replicates. Bars and error bars represent mean and SEM, respectively. Statistical
significance was calculated by one-way ANOVA and following the Tukey's test for
multiple comparison analysis. **$P < 0.01$, ***$P < 0.001$.

Corresponding author(s): Asuka Inoue

Last updated by author(s): Jun 1, 2025

Reporting Summary

Nature Portfolio wishes to improve the reproducibility of the work that we publish. This form provides structure for consistency and transparency in reporting. For further information on Nature Portfolio policies, see our Editorial Policies and the Editorial Policy Checklist.

Statistics

For all statistical analyses, confirm that the following items are present in the figure legend, table legend, main text, or Methods section.

n/a	Confirmed	
☐	☒	The exact sample size (*n*) for each experimental group/condition, given as a discrete number and unit of measurement
☐	☒	A statement on whether measurements were taken from distinct samples or whether the same sample was measured repeatedly
☐	☒	The statistical test(s) used AND whether they are one- or two-sided *Only common tests should be described solely by name; describe more complex techniques in the Methods section.*
☒	☐	A description of all covariates tested
☐	☒	A description of any assumptions or corrections, such as tests of normality and adjustment for multiple comparisons
☐	☒	A full description of the statistical parameters including central tendency (e.g. means) or other basic estimates (e.g. regression coefficient) AND variation (e.g. standard deviation) or associated estimates of uncertainty (e.g. confidence intervals)
☐	☒	For null hypothesis testing, the test statistic (e.g. *F*, *t*, *r*) with confidence intervals, effect sizes, degrees of freedom and *P* value noted *Give P values as exact values whenever suitable.*
☐	☒	For Bayesian analysis, information on the choice of priors and Markov chain Monte Carlo settings
☒	☐	For hierarchical and complex designs, identification of the appropriate level for tests and full reporting of outcomes
☒	☐	Estimates of effect sizes (e.g. Cohen's *d*, Pearson's *r*), indicating how they were calculated

Our web collection on statistics for biologists contains articles on many of the points above.

Software and code

Policy information about availability of computer code

Data collection	SoftMax Pro 7.1.2, AIS 2.5.79, Amersham Imager 680
Data analysis	GROMACS 2020.4, MODELLER 9.25, pymol 2.6.0a0, MDTraj 1.9.6, Numpy 1.21.1, Matplotlib 3.4.2, GraphPad Prism 10, ImageJ 1.53e, AAS 2.6.9, vbSPT 1.1.4 , VB-EM algorithm, Igor Pro 9, smDynamicsAnalyzer

For manuscripts utilizing custom algorithms or software that are central to the research but not yet described in published literature, software must be made available to editors and reviewers. We strongly encourage code deposition in a community repository (e.g. GitHub). See the Nature Portfolio guidelines for submitting code & software for further information.

Data

Policy information about availability of data

All manuscripts must include a data availability statement. This statement should provide the following information, where applicable:

- Accession codes, unique identifiers, or web links for publicly available datasets
- A description of any restrictions on data availability
- For clinical datasets or third party data, please ensure that the statement adheres to our policy

All data generated or analyzed during this study are available within the article, its Supplementary Information, or the Source Data file. The source data for Figs. 1–5 and Extended Data Figs. 3–10 are provided in the separate Source Data file accompanying this article. Structural data used in this study are available in the Protein Data Bank under accession code PDB: 6U1N and 7KH0. The ImageJ macro used for image preprocessing is available at https://github.com/masataka-yanagawa/

ImageJ-macro-ImageProcessingSMT, and the vbSPT algorithm is available at https://vbspt.sourceforge.net/. AAS software is available from https://eng.zido.co.jp/. Simulation input files are deposited in Zenodo at 10.5281/zenodo.15549775.

Research involving human participants, their data, or biological material

Policy information about studies with [human participants or human data](#). See also policy information about [sex, gender (identity/presentation), and sexual orientation](#) and [race, ethnicity and racism](#).

Reporting on sex and gender	Not applicable.
Reporting on race, ethnicity, or other socially relevant groupings	Not applicable.
Population characteristics	Not applicable.
Recruitment	Not applicable.
Ethics oversight	Not applicable.

Note that full information on the approval of the study protocol must also be provided in the manuscript.

Field-specific reporting

Please select the one below that is the best fit for your research. If you are not sure, read the appropriate sections before making your selection.

☒ Life sciences   ☐ Behavioural & social sciences   ☐ Ecological, evolutionary & environmental sciences

For a reference copy of the document with all sections, see [nature.com/documents/nr-reporting-summary-flat.pdf](#)

Life sciences study design

All studies must disclose on these points even when the disclosure is negative.

Sample size	No statistical method was used to determine the sample size. For NanoBiT-based GPCR assays, three independent biological replicates were performed. For single-molecule tracking analysis, data were obtained from at least 18 cells across two independent imaging sessions. Sample sizes were chosen based on prior experience and established practices in the field, and were sufficient to ensure reproducibility and to capture biologically meaningful differences.
Data exclusions	No data was systematically excluded.
Replication	In vitro experiments were independently performed two times for single-molecule tracking microscopy and at least three times for all of the other experiments. All attempts at replication were succeeded.
Randomization	Not applicable.
Blinding	No blinding was attempted or needed. There was no group allocation performed in this study.

Reporting for specific materials, systems and methods

We require information from authors about some types of materials, experimental systems and methods used in many studies. Here, indicate whether each material, system or method listed is relevant to your study. If you are not sure if a list item applies to your research, read the appropriate section before selecting a response.

Materials & experimental systems

n/a	Involved in the study
☐	☒ Antibodies
☐	☒ Eukaryotic cell lines
☒	☐ Palaeontology and archaeology
☒	☐ Animals and other organisms
☒	☐ Clinical data
☒	☐ Dual use research of concern
☒	☐ Plants

Methods

n/a	Involved in the study
☒	☐ ChIP-seq
☒	☐ Flow cytometry
☒	☐ MRI-based neuroimaging

Antibodies

Antibodies used	Primary antibodies used in this study: mouse monoclonal anti-α-tubulin (clone DM1A; Santa Cruz Biotechnology, sc-32293; 1:2000 dilution) rabbit monoclonal anti-βarr1 (clone D8O3J; Cell Signaling Technology, #12697; 1:1000 dilution) rabbit monoclonal anti-βarr2 (clone C16D9; Cell Signaling Technology, #3857; 1:1000 dilution) Secondary HRP-conjugated antibodies anti-mouse IgG (GE Healthcare, NA9310; 1:2000 dilution) anti-rabbit IgG (GE Healthcare, NA9340; 1:2000 dilution)
Validation	anti-α-tubulin (mouse monoclonal, clone DM1A, Santa Cruz Biotechnology, sc-32293) Application used: Western blot Species: human Validation: Validated for WB by the manufacturer (Santa Cruz). anti-βarr1 (rabbit monoclonal, clone D8O3J, Cell Signaling Technology, #12697) Application used: Western blot Species: human Validation: Validated for WB by the manufacturer (Cell Signaling Technology). anti-βarr2 (rabbit monoclonal, clone C16D9, Cell Signaling Technology, #3857) Application used: Western blot Species: human Validation: Validated for WB by the manufacturer (Cell Signaling Technology).

Eukaryotic cell lines

Policy information about cell lines and Sex and Gender in Research

Cell line source(s)	HEK293A cells were obtained from Thermo Fisher Scientific (Cat# R70507, RRID:CVCL_6910). These cells are derived from Homo sapiens (female). βarr1/2 knockout (KO) cells were generated from the parental HEK293A line using CRISPR/Cas9-mediated gene disruption.
Authentication	No authentication required.
Mycoplasma contamination	All cell lines used in this study were tested for mycoplasma contamination and confirmed negative.
Commonly misidentified lines (See ICLAC register)	No commonly misidentified cell lines were used.

Plants

Seed stocks	*Report on the source of all seed stocks or other plant material used. If applicable, state the seed stock centre and catalogue number. If plant specimens were collected from the field, describe the collection location, date and sampling procedures.*
Novel plant genotypes	*Describe the methods by which all novel plant genotypes were produced. This includes those generated by transgenic approaches, gene editing, chemical/radiation-based mutagenesis and hybridization. For transgenic lines, describe the transformation method, the number of independent lines analyzed and the generation upon which experiments were performed. For gene-edited lines, describe the editor used, the endogenous sequence targeted for editing, the targeting guide RNA sequence (if applicable) and how the editor was applied.*
Authentication	*Describe any authentication procedures for each seed stock used or novel genotype generated. Describe any experiments used to assess the effect of a mutation and, where applicable, how potential secondary effects (e.g. second site T-DNA insertions, mosiacism, off-target gene editing) were examined.*